KTH Electrical Engineering

Wide-angle scanning wide-band phased array antennas

ANDERS ELLGARDT

Doctoral Thesis
Stockholm, Sweden 2009

TRITA-EE 2009:017
ISSN 1653-5146
ISBN 978-91-7415-291-3

KTH School of Electrical Engineering
SE-100 44 Stockholm
SWEDEN

Akademisk avhandling som med tillstånd av Kungl Tekniska högskolan framlägges till offentlig granskning för avläggande av teknologie doktorsexamen fredagen den 8 maj 2009 klockan 13.15 i sal F3, Kungl Tekniska högskolan, Lindstedtsvägen 26, Stockholm.

© Anders Ellgardt, 2009

Tryck: Universitetsservice US AB

Abstract

This thesis considers problems related to the design and the analysis of wide-angle scanning phased arrays. The goals of the thesis are the design and analysis of antenna elements suitable for wide-angle scanning array antennas, and the study of scan blindness effects and edge effects for this type of antennas. Wide-angle scanning arrays are useful in radar applications, and the designs considered in the thesis are intended for an airborne radar antenna. After a study of the wide-angle scanning limits of three candidate elements, the tapered-slot was chosen for the proposed application. A tapered-slot antenna element was designed by using the infinitive array approach and the resulting element is capable of scanning out to 60° from broadside in all scan planes for a bandwidth of 2.5:1 and an active reflection coefficient less than -10 dB. This design was implemented on an experimental antenna consisting of 256 elements. The predicted performance of the antenna was then verified by measuring the coupling coefficients and the embedded element patterns, and the measurements agreed well with the numerical predictions. Since the radar antenna is intended for applications where stealth is important, an absorbing layer is positioned on top of the ground plane to reduce the radar cross section for the antenna's cross-polarization. This absorbing layer attenuates guided waves that otherwise lead to scan blindness, but does not adversely affect the antenna performance for the desired scan directions and frequencies. The highest frequency limit of the tapered-slot element is set by scan blindnesses. One of these scan blindnesses is found to be unique to tapered-slot elements positioned in triangular grids. This scan blindness is studied in detail and a scan blindness condition is presented and evaluated. The evaluation of the experimental antenna shows that edge effects reduce the H-plane performance of the central elements. These edge effects are further studied and characterized, by comparing the scattering parameters for finite-by-infinite arrays and infinite arrays. In this way it is possible to divide the edge effects into two categories: those caused by finite excitation, and those caused by perturbed currents due to the geometry of the edge. A finite difference time domain code with time shift boundaries is used to compute the active reflection coefficients needed to compute the scattering parameters, but this code cannot directly compute the active reflection coefficient for all the required phase shifts. Hence, an additional method is presented that makes it possible to compute arbitrary phase shifts between the elements using any numerical code with limited scan directions.

Preface

This work has been carried out at the Division of Electromagnetic Engineering, Royal Institute of Technology (KTH), Sweden. I express my gratitude to my principal supervisor Martin Norgren for his guidance and tireless proofreading of my manuscripts. I would also like to thank my other supervisors Hans Steyskal, Patrik Persson and Lars Jonsson for their help and encouragement, especially Patrik Persson who continued to aid me in my work after he left the division. Furthermore, I thank all present and former colleagues at the department for providing an inspiring atmosphere.

The thesis work is mainly done within two projects within the National Aviation Engineering Research Programme (NFFP3+ and NFFP4). In these projects KTH have had an industrial partner Saab Microwave Systems who among many things built the experimental antenna. I am very grateful for the great work done by Andreas Wikström at Saab who helped me with some of the practical problems that are otherwise neglected in academia. I would also like to acknowledge Anders Höök and Joakim Johansson at Saab for their input and encouragement.

I have used several different numerical codes during this work. The most frequently used code was the PBFDTD-code provided by Henrik Holter. Apart from the code itself, he has given me excellent support whenever I required it, thank you. I have also had the opportunity to visit FOI and use their FDTD-code written by Torleif Martin. I would like to thank Lars Pettersson and Torleif Martin for this opportunity. The friendly atmosphere at FOI made every visit enjoyable and informative.

Finally and most of all I would like to thank my family and friends. Without your support this work would not have been possible. I express my earnest gratitude to my parents and my sister for their love and support. Most of all, to my wife, Jin for her love and patience, I love you!

Anders Ellgardt
Stockholm, March 2009

List of papers

This thesis consists of a General Introduction and the following scientific papers:

I A. Ellgardt, “Study of Rectangular Waveguide Elements for Planar Wide-Angle Scanning Phased Array Antennas”. *IEEE International Symposium on Antennas and Propagation (AP-S 2005)* , Washington, U.S., July 2005

II A. Ellgardt and P. Persson, “Characteristics of a broad-band wide-scan fragmented aperture phased array antenna”. *First European Conference on Antennas and Propagation (EuCAP)*, Nice, France, November 2006

III A. Ellgardt, “Effects on scan blindnesses of an absorbing layer covering the ground plane in a triangular grid single-polarized tapered-slot array”. *IEEE International Symposium on Antennas and Propagation (AP-S 2008)*, San Diego, U.S., July 2008

IV A. Ellgardt, “A Scan Blindness Model for Single-Polarized Tapered-Slot Arrays in Triangular Grids”. *IEEE Transactions on Antennas and Propagation*, Vol. 56, No. 9, pp 2937-2942, September 2008.

V A. Ellgardt and A. Wikström, “A single polarized triangular grid tapered-slot array antenna”. Accepted for publication in *IEEE Transactions on Antennas and Propagation*, 2009

VI A. Ellgardt, “Computing return loss for arbitrary scan directions using limited scan codes for infinite phase arrays”. *Submitted to Journal January 2009*

VII A. Ellgardt and M. Norgren, “A study of edge effects in triangular grid tapered-slot arrays using coupling coefficients”. *Submitted to Journal March 2009*

The author’s contribution to the included papers

I did the main part of the work in the papers included in this thesis. Martin Norgren and Patrik Persson have helped me with proof reading of the manuscripts and made helpful suggestions, and in paper II Patrik wrote part of the numerical code used for the optimization. In paper V Andreas Wikström was responsible for the mechanical construction and he and his co-workers at Saab built the experimental antenna. Andreas also performed all the S-parameter measurements.

Contents

1 Introduction 1
- 1.1 Background 1
- 1.2 Some phased array antenna issues 2
- 1.3 Main contribution of the thesis 2
- 1.4 Thesis outline 3

2 Array theory 5
- 2.1 Planar arrays 9
- 2.2 Infinite array 12

3 Wide scan elements 17
- 3.1 Waveguide aperture element 18
- 3.2 Fragmented aperture element 19
- 3.3 Tapered-slot element 23

4 Experimental antenna 31

5 Scan blindness 37
- 5.1 Dielectric slab on top of a ground plane 37
- 5.2 Tapered-slot triangular grid scan blindness 38
- 5.3 Broadside scan blindnesses 40

6 Edge effects 43
- 6.1 Finite-by-infinite arrays 44
- 6.2 Infinite array data 47

7 Conclusions 51

8 Summary of papers 53
- 8.1 Paper I 53
- 8.2 Paper II 53
- 8.3 Paper III 54
- 8.4 Paper IV 55

8.5 Paper V 55
8.6 Paper VI 55
8.7 Paper VII 56

Bibliography **57**

Chapter 1

Introduction

1.1 Background

Phased array antennas consist of multiple fixed antenna elements, which can be excited differently in order to control the radiation pattern. In a basic phased array the elements are fed coherently and at all elements phase shifters or time-delays are used to scan the beam to desired directions in space. Uniformly excited arrays with a linear phase shift will create a directive beam that can be repositioned electronically by changing the phase shifts. If the amplitude and phase of each element can be controlled individually the beam of the array can be formed to more general patterns. This technique is called beamforming and can be used to suppress side lobes, to create radiations pattern nulls in certain directions, or to create application specific patterns [1].

Phased array antenna systems can be used in numerous applications, where one of the oldest is radar systems. The first phased array radar system dates back to the second world war, and today phased array radar systems are increasingly used on naval ships and aircrafts. Modern phased array radar systems can perform several tasks simultaneously, like keeping track of ground and air targets while at the same time communicating with other units.

The second oldest application is radio astronomy, where phased arrays can be used by themselves or as a feed for a large reflector antenna. An ongoing project that may use phased arrays in both these configurations is the Square Kilometre Array (SKA) [2, 3]. SKA will probe the gaseous component of the early Universe, thereby addressing fundamental questions in research on the origin and evolution of the Universe. This is an enormous international project in which the largest radiotelescope in the world will be built.

An application on the rise is mobile communication systems, where beamforming can be used for avoiding overlap between communication cells, changing the coverage during the day or to increase the range for a single base station. Phased arrays are also used for synthetic apertures, broadcasting, and radio frequency identification (RFID) readers.

1.2 Some phased array antenna issues

Phased array antennas are cumbersome to analyze directly due to their large size in terms of wavelengths. An additional problem is that the arrays often are densely packed, which yields strong coupling between the elements. As a consequence of the strong coupling the active reflection coefficient changes with excitation, and therefore multiple calculations with different excitations are always required to fully characterize an antenna. To design a phased array antenna one is usually required to either disregard the coupling between the elements or to assume that the antenna elements behave as if they were positioned in an infinite array. The infinite array approximation is usually the best choice for analyzing large dense arrays, for which the approximation is good for the central elements. Several textbooks on the subject are available for the antenna engineers, and the author's personal favorites are [4–7].

A recent progress in phased array research is to solve the fields for the whole antenna in one simulation, either using clever numerical codes that utilize characteristic currents to reduce the number of unknowns, or using a method that approximates the finite array with a finitely excited infinite array with corrections for the edges [8–15]. Another approach is to solve the numerics by brute force, using large clusters of computers [16, 17], or by dividing the array into subdomains which are linked together by the boundary conditions [18, 19]. All these methods allows the engineer to solve larger and more complex problems, and the increased accuracy of the numerical methods reduces the need for measurements.

1.3 Main contribution of the thesis

In this thesis, the emphasis has been on reducing the complexity of the phased array antennas, and on trying to answer why specific elements work the way they do and how different design solutions affect the antenna parameters. Much of the work is done by using the infinite array approximation. The choice is partly made out of necessity, due to limited numerical resources, but also since it is a powerful method that fits the aim of the thesis.

The aim was to design and study wide-angle scanning wide-band planar phased arrays, and a specific goal was to design an antenna element for a phased array radar antenna. This antenna was intended to be carried by a military aircraft, which requires low radar cross section and lightweight construction.

In order to reach the goal, a number intermediate goals were determined, which can be summarized as:

- Investigate and find suitable antenna elements for wide-angle scanning arrays.
- Design an antenna element for a wide-angle scanning phased array radar antenna.
- Build an experimental antenna based on the design of the wide-angle scanning antenna element.

- Investigate and model scan blindnesses and surface waves for the chosen design.
- Investigate and characterize edge effects for the chosen design.

1.4 Thesis outline

Chapter 2 gives a brief overview of the basic phased array theory for finite and infinite arrays.

In chapter 3, three types of elements for wide-angle scanning arrays are described and discussed, namely: the waveguide aperture element, the fragmented aperture element, and the tapered-slot element. The tapered-slot element is chosen for the experimental antenna and the outline for the design of this element is given.

The experimental antenna consists of 256 elements. It was built by Saab Microwave Systems and the evaluation of the results is given in chapter 4. The performance of the experimental antenna is shown to agree well with the numerical results and the active return loss and embedded element patterns are presented.

The tapered-slot element designed for the experimental antenna displays three types of scan blindnesses. It is important to characterize these scan blindnesses since they limit the bandwidth and wide-angle scanning performance of the antenna. In chapter 5 a brief description is given of the scan blindness phenomena and the different scan blindnesses types.

In chapter 6 the edge effects are studied for an antenna similar to the experimental antenna. The arrays studied are finite in one direction only, which simplifies the analysis and makes it possible to study the effect of a single edge. The edge effects are studied by comparing the coupling coefficients for a finite-by-infinite array and an infinite array. At the end of this chapter a method, based on a finite difference time domain code using time shift boundaries, is presented on how to compute the active reflection coefficient for a phase shift that moves the main beam outside visual space. These phase shifts are crucial for computing the infinite array coupling parameters.

Chapter 7 contains a summary of the thesis and general conclusions, and chapter 8 contains a summary of the individual papers.

Chapter 2

Array theory

This chapter provides an introduction for readers unfamiliar with the basic concepts of planar phased array antennas and infinite arrays. The focus will be on two questions that are of key importance. The first is: how does the antenna radiate, and the second, how efficient is the antenna. There are many other questions that are also interesting to answer, regarding the ease and cost of manufacturing, the radar cross section, the size and weight of the antenna, but without an answer to the two first questions one cannot evaluate the performance of an antenna.

In the idealized antenna design case, we consider antennas in free space. For such a case we can partition the surrounding space of an antenna into two regions, the near field region and the far field region. The far field region is the region where the angular field distribution of an antenna is essentially independent of the distance from a specified point in the antenna region [20]. A prerequisite for this condition is that the fields in the far field region are the radiated fields from the antenna. A radiated field from a finite antenna is a wave whose amplitude is proportional to the inverse of the distance from the source. That means that the power density of the field decreases as inverse of the square of the distance to the source, and that the power of the radiated fields passing through a sphere enclosing the element is constant, regardless of the radius of the sphere. In the far field region the field distribution of an antenna is called the radiation pattern, which can be expressed in several ways depending on how the surroundings of the antenna are treated. One type of radiation pattern is the embedded element pattern, which is practical when the antenna consists of a group of antenna elements. The embedded element pattern is the radiation pattern of an element in a system of several elements when this element is connected to a generator with internal impedance equal to the characteristic impedance of the port of the element and all other element ports are terminated with their characteristic impedance.

An important usage of the embedded element patterns, $\boldsymbol{f}_n$, is that they can be used to describe the electric far field, $\boldsymbol{E}$, of an array antenna. The electric far field in a field point, $\boldsymbol{r}$, from a sequence of antenna elements, at the positions r_n,

$n = 1, 2...$, has the form

$$\boldsymbol{E}(\boldsymbol{r}) = \sum_{n=1}^{N} A_n \boldsymbol{f}_n(\theta_n, \phi_n) \frac{\mathrm{e}^{-\mathrm{j}kR_n}}{R_n}. \tag{2.1}$$

Here, N is the number of elements, A_n is the incident voltage at the port of element n, θ_n and ϕ_n are the individual elements spherical local description to the field point $\boldsymbol{r}$, and k is the free space wavenumber. Furthermore the distance between element n and the field point is denoted R_n, where

$$R_n = |\boldsymbol{r} - \boldsymbol{r}'_n|\,. \tag{2.2}$$

In Eq. (2.1), $\boldsymbol{r}$, has to be in the joint far field region, which is the intersection of the far field regions of all the antenna elements. From the field obtained in Eq. (2.1) we can compute the radiation pattern of the antenna elements as a group. The radiation pattern expresses in which direction the array antenna radiates and where zeros or non-radiation directions are localized. However, it is not sufficient to describe the efficiency or the matching properties of the array antenna.

The efficiency of an antenna is partly determined by how much of the incident power that is reflected at the antenna port, and partly by the material properties of the antenna array. The first type of loss is quantified by the active reflection coefficient, Γ_m, the amplitude of the reflected wave at port m, which can be calculated from quantities called the scattering parameters (S-parameters). An S-parameter, S_{mn}, relates the amplitude of an incident wave at port n, A_n, to the the amplitude of the outgoing wave at port m. It is usually the preferred quantity to measure in experimental antennas and is therefore chosen to represent coupling in this thesis. The relation between Γ_m and A_n is expressed as

$$\Gamma_m = \sum_{n=1}^{N} S_{mn} A_n. \tag{2.3}$$

With the knowledge of $\boldsymbol{f}_n$ and S_{mn} we can obtain estimates of the array performance. However, for large arrays it is computationally costly to determine the embedded element patterns and the S-parameters. A way to circumvent this problem is to simplify the theory. A simplification can be obtained for the E-field in the far field region of the array antenna. The electric-field given by Eq. (2.1) is valid for a region that is larger than the far field region for the antenna elements as a group. In Figure 2.1 this is illustrated for four elements, where the boundary between the far field region and the near field region of the individual elements are conceptually depicted as circumscribing circles. To achieve a radiation pattern for this antenna the field point must be farther away from the elements, so that the fields emitted from the antenna elements seem to come from the same direction thus, $\theta_n \approx \theta$ and $\phi_n \approx \phi$. This approximation holds when the antenna elements are located much closer to the origin than the field point, in which case the distance R_n

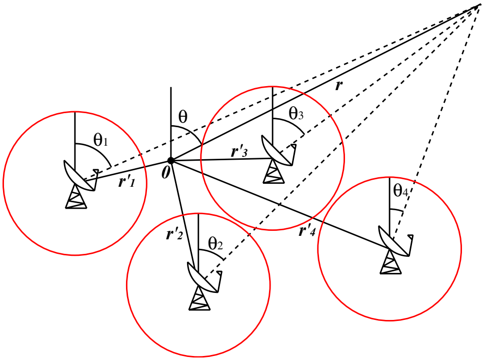

Figure 2.1: The field point $\boldsymbol{r}$ is in the far field regions for the individual antenna elements but not in the far field region of the antenna elements as a group.

between the source and field point can be approximated with a Taylor series. In the far-field zone the exponential terms in Eq. (2.1) describes how the phase changes with position in space. Here the difference in phase between elements is important, which requires two terms in the Taylor series. The distance is then simplified to

$$R_n \approx r - \hat{\boldsymbol{r}} \cdot \boldsymbol{r}'_n = \left\{ \hat{\boldsymbol{r}} = \frac{\boldsymbol{k}}{k} \right\} = r - \frac{\boldsymbol{k}}{k} \cdot \boldsymbol{r}'_n, \tag{2.4}$$

where $\boldsymbol{k}$ is defined as

$$\begin{aligned} \boldsymbol{k} &= k_x \hat{\boldsymbol{x}} + k_y \hat{\boldsymbol{y}} + k_z \hat{\boldsymbol{z}}, \\ k_x &= k \sin\theta \cos\phi, \\ k_y &= k \sin\theta \sin\phi, \\ k_z &= k \cos\phi. \end{aligned} \tag{2.5}$$

The denominator of the last term in Eq. (2.1) describes how the amplitude of the far field decreases with distance. In the far field zone the different distances to the elements will have a negligible effect on the magnitude of the individual element contributions, whereby it is sufficient to approximate

$$\frac{1}{R_n} \approx \frac{1}{r}. \tag{2.6}$$

The array antenna can be seen as an aperture where the elements are sample points. An efficient way to sample the aperture is to use identical elements placed in a periodic pattern, which yields similar embedded element patterns for the elements in the center of the antenna. Hence, for large array antennas it is a good approximation that the embedded element patterns are identical for all elements.

$$\boldsymbol{f}_n(\theta, \phi) = \boldsymbol{f}_0(\theta, \phi) \tag{2.7}$$

Using approximation (2.4), (2.6), and (2.7) we can in Eq. (2.1) move out the element pattern from the summation, by which the far-field becomes a product of an element pattern, a spherical wave emitted from the origin, and a factor depending only on the inter element spacing. This factor is called the array factor and unlike the element pattern it varies rapidly with the direction for large arrays.

$$\boldsymbol{E} = \underbrace{\boldsymbol{f}_0(\theta,\phi)}_{\text{element pattern}} \frac{\mathrm{e}^{-\mathrm{j}kr}}{r} \underbrace{\sum_{n=1}^{N} A_n \mathrm{e}^{\mathrm{j}\boldsymbol{k}\cdot\boldsymbol{r}'_n}}_{\text{array factor}} \tag{2.8}$$

Equation (2.8) is a considerable simplification of Eq. (2.1) from the analytical and computational perspective, since we only need to know one embedded element pattern.

To change the radiation pattern we use the excitation, A_n. The number of available synthesis techniques for the excitation is large, and the best choice depends on the application. One of the most basic excitations is when the amplitude of the excitation is uniform $|A_n| = A$ and only the phase is changed to form a radiation pattern. This type of excitation can produce directive narrow beams suitable for many applications. Let's derive such an excitation for an array where one of the elements is positioned at the origin with its excitation set to A, then term in the array factor corresponding to this element is equal to A. To maximize the array factor for a specific direction, say $\boldsymbol{k}_0$, the phase of A_n must be chosen so that all the remaining terms in the array factor in this direction are equal to A. An excitation that fulfills this requirement is

$$A_n = A\mathrm{e}^{-\mathrm{j}\boldsymbol{k}_0\cdot\boldsymbol{r}'_n}. \tag{2.9}$$

For the case when all the elements have identical element patterns, Eq. (2.9) is the optimal excitation to achieve the maximum gain. This excitation is a special case of the more general maximum-array-gain theorem, which holds for nonidentical elements, see e.g. [7, Ch. 1]. For the excitation given by Eq. 2.9, the far field becomes

$$\boldsymbol{E} = \boldsymbol{f}_0(\theta,\phi)\frac{\mathrm{e}^{-\mathrm{j}kr}}{r} A \sum_{n=1}^{N} \mathrm{e}^{\mathrm{j}\boldsymbol{k}'\cdot\boldsymbol{r}'_n}, \tag{2.10}$$

where $\boldsymbol{k}' = \boldsymbol{k} - \boldsymbol{k}_0$.

Let's consider an example, where a linear array antenna with N elements and an element spacing a is excited with the excitation (2.9). Then the antenna's main beam will be directed $\pi/2-\theta_0$ from the array axis, see Fig. 2.2. For this direction the phase shifts between the elements compensate for the difference in phase caused by the different lengths the waves travel to the far field point. These phase shifts can be realized either by delaying the signal between the elements or by using phase shifters that change the phase of the excitation. A time delay between elements n and $n+1$ is equal to the time the wave travels the distance $\boldsymbol{k}_0 \cdot \boldsymbol{r}'_n - \boldsymbol{k}_0 \cdot \boldsymbol{r}'_{n+1} = a\cos\theta_0$. The

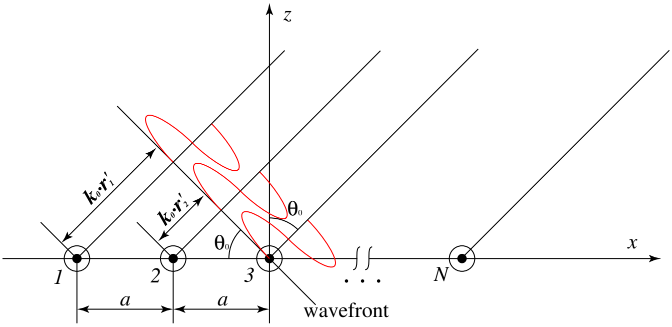

Figure 2.2: Linear array with N elements steered out to θ_0 from broadside scan.

time delay for a specific scan direction is frequency independent unlike the phase shift that changes with frequency. Therefore, if phase shifters are used the direction θ_0 of the beam will also be a function of the frequency. This effect is unsuitable for broadband applications, but could be used to steer the beam in narrow band applications.

We have above introduced the basic key quantities, the embedded element pattern, the excitation, the S-parameters, and the active reflection coefficient. These key parameters will play an important role in this thesis. We will know continue to study the excitation of the planar array and then study how the active reflection coefficient is linked to the embedded element pattern for an infinite array.

2.1 Planar arrays

The antennas studied in this thesis are planar and the element spacing is periodic. Planar arrays with periodic spacing will have a periodic excitation, and in this section we explain the periodicity of the excitation and show how it affects the radiation pattern.

The elements in the array are positioned in the xy-plane with the normal, $\hat{\boldsymbol{n}}$, chosen in the positive z-direction. Two primitive vectors called $\boldsymbol{a_1}$ and $\boldsymbol{a_2}$ are used to describe the element positions in the grid. The first of the primitive vectors, $\boldsymbol{a_1}$, is chosen to be parallel to the x-axis and the second primitive vector, $\boldsymbol{a_2}$, is directed with the angle γ from the x-axis in the xy-plane, see Fig. 2.3. These primitive vectors are denoted

$$\begin{aligned} \boldsymbol{a_1} &= a\hat{\boldsymbol{x}}, \\ \boldsymbol{a_2} &= c\hat{\boldsymbol{x}} + b\hat{\boldsymbol{y}}, \\ c &= \frac{b}{\tan\gamma}. \end{aligned} \tag{2.11}$$

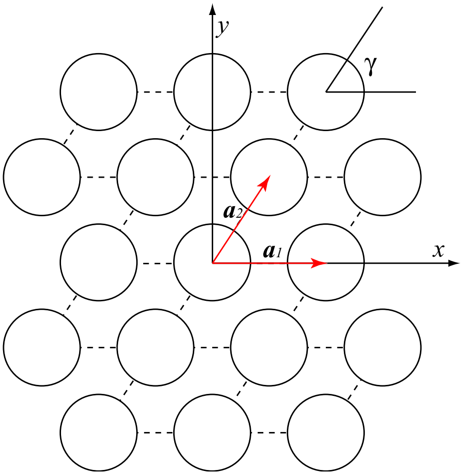

Figure 2.3: General planar array structure given by the primitive vectors $\boldsymbol{a_1}$ and $\boldsymbol{a_2}$. The circles represent antenna elements.

We will now show that when the elements are configured in periodic patterns there are several different excitations that have identical radiation patterns. Consider that the element positions are given by Eq. (2.11), then the term in the array factor corresponding to element n becomes

$$A_n \mathrm{e}^{\mathrm{j}\boldsymbol{k}'\cdot\boldsymbol{r}'_n} = A_n \mathrm{e}^{\mathrm{j}\boldsymbol{k}'\cdot(p(n)\boldsymbol{a_1}+q(n)\boldsymbol{a_2})}, \tag{2.12}$$

where q and p are integers that together with the primitive vectors describe the position of element n.

As concluded above, the array factor has a maximum when the exponential terms are equal for all values of n. This occurs when $\boldsymbol{k}_0 = \boldsymbol{k}$ but also for other values of $\boldsymbol{k}_0$. All vectors $\boldsymbol{k}'$ such that

$$\mathrm{e}^{\mathrm{j}\boldsymbol{k}'\cdot(p(n)\boldsymbol{a_1}+q(n)\boldsymbol{a_2})} = 1 \tag{2.13}$$

will result in the same radiation pattern, due to the periodicity of the grid and the exponential function. The orthogonal components of $\boldsymbol{k}'$ with respect to the normal can be expressed as

$$\boldsymbol{k}'_\perp = p'\boldsymbol{b_1} + q'\boldsymbol{b_2}, \tag{2.14}$$

where

$$\boldsymbol{b_1} = 2\pi\frac{\boldsymbol{a_2}\times\boldsymbol{n}}{\boldsymbol{a_1}\cdot(\boldsymbol{a_2}\times\boldsymbol{n})} = 2\pi\left(\frac{1}{a}\hat{\boldsymbol{x}} - \frac{c}{ab}\hat{\boldsymbol{y}}\right) \tag{2.15}$$

$$\boldsymbol{b_2} = 2\pi\frac{\boldsymbol{a_1}\times\boldsymbol{n}}{\boldsymbol{a_2}\cdot(\boldsymbol{a_1}\times\boldsymbol{n})} = 2\pi\frac{1}{b}\hat{\boldsymbol{y}}. \tag{2.16}$$

The vectors $\boldsymbol{b_1}$ and $\boldsymbol{b_2}$ are the reciprocal primitive vectors of the array grid, and q' and p' are integers. A linear phase shift of any excitation will translate the array factor in the $k_x k_y$-plane, and since the array factor is periodic the far field pattern will be unchanged, e.g. if $\boldsymbol{k}_0 = \boldsymbol{0}$ is changed to $\boldsymbol{k}_0 = p'\boldsymbol{b_1} + q'\boldsymbol{b_2}$. In Fig. 2.4 a phase diagram is shown for $\boldsymbol{k}$, this diagram is usually called a grating lobe diagram. The dot in the center of the solid circle represents the main beam direction when $\boldsymbol{k}_0 = \boldsymbol{0}$, and the dot in the center of the dashed circles are the other maxima directions, due to the periodicity. The dot denoted $\boldsymbol{k}_{0,0}$ corresponds to the main beam direction when $\boldsymbol{k}_0 = k_{x0}\hat{\boldsymbol{x}} + k_{y0}\hat{\boldsymbol{y}}$, and is similarly translated for the other maxima. The solid circle has a radius equal to k and encloses the directions corresponding to visual space. Phase shifts outside this circle corresponds to directions for which θ is imaginary and the element pattern is zero. The dashed circles represent the possible locations of the other array factor maxima when (k_{x0}, k_{y0}) are in visual space.

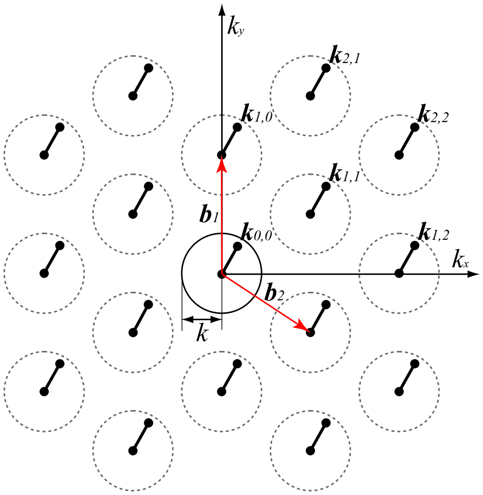

Figure 2.4: Grating lobe diagram for the array grid depicted in Fig 2.3.

For high frequencies the circles in the grating lobe diagram will overlap and it is possible to position more than one array factor maxima in visual space. The additional radiating beams are called grating lobes. The occurrence of grating lobes decreases the directivity of the antenna, and can also cause sudden changes in the active impedance and thereby further reduce the absolute gain of the antenna. Grating lobes are an aliasing effect due to a too sparse sampling of the surface covered by the antenna.

2.2 Infinite array

The previous theory describes the periodicity of the excitation of a planar array antenna and how it radiates. To put this theory to work, one needs to know the embedded element patterns and S-parameters for an array antenna, and to compute these quantities numerical methods are required. Due to the size of the computational domain it is difficult to analyze large planar arrays by numerical methods. Therefore, simplifications are needed, and a good starting point is the infinite array. When the infinite array is fed with a uniform amplitude and a linear phase shift the geometry can be reduced to a unit cell with quasi-periodic boundaries. This is a result of the Floquet theorem and the excitation used is referred to as the Floquet excitation.

In this section we will study the sources in the infinite array, when it is excited with a Floquet excitation, and show that the radiated field consists of a limited number of plane waves propagating from the antenna. Furthermore, we will discuss the relationship between the active reflection coefficient and the S-parameters and the relationship between the active reflection coefficient and the embedded element pattern for an infinite array.

Let's start with the source terms for an infinite array. Consider that element n is excited with a unit amplitude, which yields a source term in the array of the form $f\left(x-x_n, y-y_n\right)$. Furthermore, if the array is excited with a Floquet excitation, the source term will be a superposition of all the element contributions i.e. a current component can be written as

$$i\left(x,y\right)=\sum_{p,q} f\left(x-x_{pq}, y-y_{pq}\right)\mathrm{e}^{-\mathrm{j}k_{x0}x_{pq}-\mathrm{j}k_{y0}y_{pq}}, \tag{2.17}$$

where

$$x_{pq}=\left(p\boldsymbol{a_1}+q\boldsymbol{a_2}\right)\cdot\hat{\boldsymbol{x}} \tag{2.18}$$

$$y_{pq}=\left(p\boldsymbol{a_1}+q\boldsymbol{a_2}\right)\cdot\hat{\boldsymbol{y}}. \tag{2.19}$$

As a consequence of the Floquet theorem the source terms and fields in the array have the same periodicity as the Floquet excitation. The array structure can be divided into unit cells, which if translated using integers of the primitive lattice vectors, reproduce the infinite array. The fields at one boundary of the unit cell will be identical to the fields at the opposing boundary multiplied with the phase shift in that direction. In numerical codes using periodic boundaries with phase shifts, this periodicity is imposed explicitly.

As an introduction to the Floquet modes we will derive the Floquet series expansion of a the current component $i(x,y)$. The Fourier transform of the source current is

$$\tilde{i}\left(k_x,k_y\right)=\frac{1}{4\pi^2}\int_{-\infty}^{\infty}\int_{-\infty}^{\infty} i\left(x,y\right)\mathrm{e}^{\mathrm{j}k_x x+\mathrm{j}k_y y}\,\mathrm{d}x\,\mathrm{d}y \tag{2.20}$$

with inverse transform

$$i\left(x,y\right)=\int_{-\infty}^{\infty}\int_{-\infty}^{\infty}\tilde{i}\left(k_x,k_y\right)\mathrm{e}^{-\mathrm{j}k_x x-\mathrm{j}k_y y}\,\mathrm{d}k_x\,\mathrm{d}k_y. \tag{2.21}$$

Inserting Eq. (2.17) into (2.20) gives

$$\tilde{i}\left(k_x,k_y\right)=\tilde{f}\left(k_x,k_y\right)\sum_{p,q}\mathrm{e}^{\mathrm{j}\boldsymbol{k}'\cdot\left(p\boldsymbol{a_1}+q\boldsymbol{a_2}\right)}. \tag{2.22}$$

The sum in Eq. (2.22) is the array factor for an infinite array, which is equal to zero except at discrete scan angles. This can be shown by using Poisson's summation formula, whereby the sum becomes

$$\begin{aligned}\sum_{p,q}\mathrm{e}^{\mathrm{j}\boldsymbol{k}'\cdot\left(p\boldsymbol{a_1}+q\boldsymbol{a_2}\right)}&=\\ 4\pi^2\sum_{p,q}\delta\big(\boldsymbol{k}'\cdot\boldsymbol{a_1}+2\pi p\big)\,\delta\big(\boldsymbol{k}'\cdot\boldsymbol{a_2}+2\pi q\big)&=\\ \frac{4\pi^2}{ab}\sum_{p,q}\delta(k_x-k_{xpq})\,\delta(k_y-k_{ypq})&\end{aligned} \tag{2.23}$$

where $\delta(x)$ is the delta Dirac function and

$$k_{xpq}=k_{x0}+(p\boldsymbol{b_1}-q\boldsymbol{b_2})\cdot\hat{\boldsymbol{x}} \tag{2.24}$$

$$k_{ypq}=k_{y0}+(p\boldsymbol{b_1}-q\boldsymbol{b_2})\cdot\hat{\boldsymbol{y}}. \tag{2.25}$$

Now, if Eq. (2.22) and (2.23) are inserted into Eq. (2.21), we obtain the Floquet series expansion

$$i\left(x,y\right)=\frac{4\pi^2}{ab}\sum_{p,q}\tilde{f}\left(k_{xpq},k_{ypq}\right)\mathrm{e}^{-\mathrm{j}k_{xpq}x-\mathrm{j}k_{ypq}y}. \tag{2.26}$$

Sources of this form excite an electric field that can be written in the following form for positive z above the sources [7, Ch. 2]

$$\boldsymbol{E}(x,y,z)=\sum_{pq}\boldsymbol{C}_{pq}\mathrm{e}^{-\mathrm{j}\left(k_{xpq}x+k_{ypq}y+k_{zpq}z\right)}, \tag{2.27}$$

where $\boldsymbol{C}_{pq}$ is a complex vector and

$$k_{zpq}=\sqrt{k^2-k_{xpq}^2-k_{ypq}^2}. \tag{2.28}$$

The terms in Eq. (2.27) are called Floquet modes. These modes can be divided into TE and TM-modes but here they are for brevity denoted $\boldsymbol{C}_{pq}$. These modes are plane waves that propagate from the plane of the array when k_{zpq} is real, and are evanescent when k_{zpq} is imaginary, which leads to some interesting results. For example, it is possible to choose a phase shift for the array where no beam propagates, which happens when (k_x, k_y) are outside of all circles in the grating lobe diagram in Fig. 2.4. With such a phase shift, the incident power applied at the ports of the antenna elements must be reflected back to the ports or dissipated in the antenna due to losses. This effect would be impossible if the antenna elements within the array did not couple to each other [21].

The active reflection coefficient for an element in an infinite array is closely related to the set of S-parameters, since if one of the two are known the second can be calculated. Given that the array is excited with a Floquet excitation the active reflection coefficient for element m is

$$S'^{\mathrm{FL}}(\psi_1, \psi_2) = \sum_{p,q} S_{m,n(p,q)} \mathrm{e}^{-\mathrm{j}p\psi_1 - \mathrm{j}q\psi_2}, \tag{2.29}$$

where

$$\psi_1 = \boldsymbol{k} \cdot \boldsymbol{a}_1 = k_x a \tag{2.30}$$
$$\psi_2 = \boldsymbol{k} \cdot \boldsymbol{a}_2 = k_x c + k_y b. \tag{2.31}$$

This is a two dimensional Fourier series in which the Fourier coefficients, the scattering parameters, are given by

$$S_{m,n(p,q)} = \frac{1}{4\pi^2} \int_{-\pi}^{\pi} \int_{-\pi}^{\pi} S'^{\mathrm{FL}}(\psi_1, \psi_2) \mathrm{e}^{\mathrm{j}p\psi_1 + \mathrm{j}q\psi_2} \, \mathrm{d}\psi_1 \, \mathrm{d}\psi_2. \tag{2.32}$$

The active reflection coefficient, S'^{FL}, is almost always calculated numerically using periodic boundary conditions with phase shifts. By the above Fourier transform we can calculate the S-parameters for the infinite array. Once the S-parameters are known, we use Eq. (2.3) to calculate the active reflection coefficient for arbitrary excitations.

As mentioned earlier, for a specific phase shift the scan direction will change with frequency. Therefore, when analyzing the performance of an element it is usually more convenient to express the active reflection coefficient as a function of the scan direction.

$$\Gamma^{\mathrm{FL}}(\theta, \phi) = S'^{\mathrm{FL}}(\psi_1, \psi_2). \tag{2.33}$$

The active reflection coefficient, Γ^{FL}, is related to the power gain pattern (also known as absolute gain pattern) for an element in the infinite array [22]. A prerequisite is that the elements are lossless and positioned in a sufficiently dense grid in terms of wavelength, so that only one Floquet mode at a time can be excited. Then the power gain pattern is given by

$$g(\theta, \phi) = \frac{4\pi A_{\mathrm{uc}}}{\lambda^2} \cos(\theta) \left(1 - \left|\Gamma^{\mathrm{FL}}(\theta, \phi)\right|^2\right), \tag{2.34}$$

where A_{uc} is the area of the unit cell, and λ is the wavelength in free space. The power gain pattern is equal to the square of the absolute value of the embedded element pattern

$$|\boldsymbol{f}(\theta, \phi)| = \sqrt{g(\theta, \phi)}. \tag{2.35}$$

In most synthesis of antenna patterns, one is interested in a power pattern, whereas the phase changes within the pattern are of minor interest. Since for the infinite array all elements have the same embedded element patterns, the phase information is basically redundant. By using Eq. (2.32) and Eq. (2.35) for frequencies when only one Floquet mode can propagate, it is possible to answer the two fundamental questions for the infinitive array.

When the array is finite both the coupling coefficients and the embedded element patterns change with respect to the infinite array case. Such perturbations of the infinite array solution are called edge effects. Sources in the infinite array consists of superimposed element sources $f\,(x - x_n, y - y_n)$ that represent the source in the array when only one element is excited with $A_n = 1$. The element sources extend over many antenna elements and are responsible for the coupling between elements and the embedded element patterns. When the array is truncated, so are these source terms; one could see this as making the effective radiating aperture for the edge antenna element smaller. A smaller aperture will in general result in a broader element pattern and therefore the edge element element patterns will in general be broader than the infinite array patterns.

Chapter 3

Wide scan elements

In this thesis three types of elements are studied, waveguide aperture elements, fragmented aperture elements, and tapered-slot elements. These elements have different properties. Compared to the other elements the waveguide aperture elements are narrow band but have been shown to be capable of wide scan angles. The fragmented aperture antenna is a thin wide-band antenna, but lacks the wide-angle performance. The tapered-slot element is a broad-band element that has shown good scan angle performance, but it is bulky. In this chapter the elements are assumed to be positioned in a very large array so that the central elements can be approximated by an element in an array antenna of infinite extent. This simplifies the design since only a unit cell with periodic boundaries needs to be considered.

In the first project, NFFP3+, the goal was to find an array element that was capable of scanning out to 75° from broadside with a bandwidth of 1.4:1. Here, bandwidth is defined as $f_\mathrm{h}/f_\mathrm{l}$:1, where f_h and f_l are the highest and lowest frequency limit for which the active reflection coefficient is less than -10 dB for all scan directions within the scan cone defined by θ_max.

A literature study was made [23] and three types of elements were chosen as candidates: waveguide aperture elements, stacked patch elements and tapered-slot elements. There were no elements that fully met the desired characteristics. However, there exist element designs that fulfill the bandwidth condition or the wide-scan condition but not both. Bandwidth and maximum scan-angle are conflicting design criteria and in the literature most elements that are capable of wide-scan angles are designed for a small frequency band; there are even cases when the chosen performance parameters, e.g. the active reflection coefficient or the active impedance, are only calculated for a single frequency. Phased array elements that are considered mainly as broadband elements may be suitable for wide angle scanning if the bandwidth is reduced; the tapered-slot element is such an element.

An apparent problem when we evaluated the existing elements is that there are no objective performance measure for wide-angle scanning phased array elements. In the technical report [24] three performance measures were compared for waveguide apertures. We found that the average reflected power over the scan range normalized to unit input power was a good measure to evaluate wide-angle scanning performance. The average reflected power over the scan range is defined as

$$R_{\mathrm{pw}}(f) = \frac{1}{2\pi\left(1-\cos\theta_{\max}\right)}\int_0^{2\pi}\int_0^{\theta_{\max}} |\Gamma(\theta,\phi,f)|^2 \sin\theta \,\mathrm{d}\theta\,\mathrm{d}\phi, \tag{3.1}$$

where θ and ϕ denote the scan direction in spherical coordinates, $\theta_{\max}$ the maximum scan angle, and $|\Gamma|^2$ the return losses, i.e. the power reflected back into the antennas port relative the incident power.

3.1 Waveguide aperture element

Waveguide aperture element can with irises, dielectric slabs above the apertures, and dielectric loading be match for very wide-scanning. During the 60's and 70's the waveguide aperture elements and their wide-scanning performance were the subject of many papers, see e.g. [4, 25–28], but these elements have also been studied in more recent papers [29–31]. A circular waveguide design capable of scanning out to 70° from broadside was presented in [31], and a square waveguide element with irises [25] has been shown to be capable of 60° scan from broadside. The main problem with these elements is that they have small bandwidths.

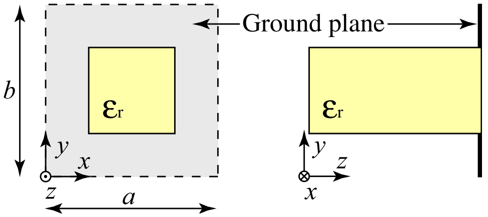

Figure 3.1: The small square waveguide aperture element.

In paper I [32], which is a condensed version of the technical report [24], we studied the performance of the basic waveguide aperture element. Three apertures were chosen for this purpose, two square waveguides capable of dual polarization and a single polarized rectangular waveguide. The elements are positioned in a square grid with the element spacing $a = b = \lambda_{\mathrm{h}}/2$ where λ_{h} is the free space wavelength at f_{h} the highest frequency considered. To reduce the size of the waveguide it is filled with a dielectric material. The size of the waveguide and the value of dielectric constant are chosen so that the second waveguide mode starts to propagate when $f = f_{\mathrm{h}}$. The cross section of the square waveguides are chosen so that for the first waveguide the cross section is close to the size of the unit cell and for the second waveguide the cross section is one fourth of the unit cell area, see Fig. 3.1. The cross section of the rectangular waveguide is chosen so that the width is the same as the large square waveguide, and the height is chosen slightly smaller than the small waveguide. The elements are excited with the first waveguide mode and this mode is matched by choosing a susceptance (conceptually) placed a distance $\lambda/2$ from the aperture and by changing the transmission line characteristic impedance (or more correctly wave impedance) to a new value. For the square waveguides the orthogonal mode is terminated by a load with the same value as the chosen characteristic impedance, again a distance $\lambda/2$ from the aperture. The susceptance and impedance were then chosen by minimizing the average reflected power (3.1) for one frequency using nonlinear programming.

Before the matching the largest waveguide was the best matched element for all scan directions. However, after the matching the smallest waveguide was better matched and had lower average reflected power over the scan range, see Fig. 3.2. The reason for the worse match of the large waveguide was that when the beam was scanned out in the diagonal plane the excited mode was to a greater degree reflected back to the orthogonal mode. The active reflection coefficients for the small waveguide and the rectangular waveguide were very similar, and the average reflected power was essentially the same. For these elements the active reflection coefficient was, after matching, similar to that of an infinite magnetic current sheet [33] that is perfectly matched for broadside scan.

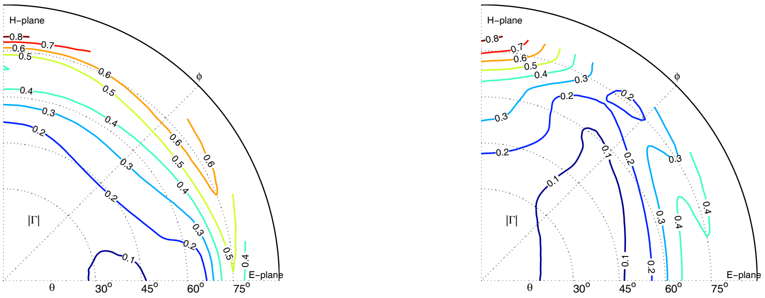

(a) large square waveguide

(b) small square waveguide

Figure 3.2: Contour plots of $|\Gamma|$ for the waveguide apertures matched by minimizing R_{pw}, $f = 2.6$ GHz. The antennas are considered to be well matched when $|\Gamma| < 0.3 \approx -10$ dB.

3.2 Fragmented aperture element

The average reflected power, as given in Eq. (3.1) would work well as a cost function to design wide-angle scanning array elements. However, it requires that Γ is known for many scan directions. For complex antenna elements it is time consuming to compute the average reflected power, which makes it practically impossible to use this quantity as a cost function to design an element. A simplified procedure for design is to choose a few scan directions that are assumed to give a good picture of the performance of the antenna. The directions chosen are often broadside scan $\theta = 0°$ and the maximum chosen scan angle $\theta = \theta_{\max}$ for the E plane and H plane. This strategy often works well because the active impedance for the maximum scan angle for the E plane and the H plane is close to the highest and lowest active impedance values for the antenna, e.g. for an infinite current sheet [33] $Z_{\mathrm{E-plane}}(\theta)/Z_0 = (Z_{\mathrm{H-plane}}(\theta)/Z_0)^{-1}$ where Z_0 is the active impedance for broadside scan.

In [34] fragmented aperture elements were designed using a genetic algorithm. The genetic algorithm is used to find the antenna geometry with the minimum reflected power for broadside scan and the maximum chosen scan angle for the E plane and H plane. The basic geometry of the fragmented aperture element is a pattern consisting of metal pixels, see Fig. 3.3. This pixel pattern is positioned on top of a dielectric slab backed by a ground plane and fed in the middle of the element with a discrete point source. Björn Thors et al. designed antenna elements by using the method presented in [34] which were capable of bandwidths of at least one octave when scanned within 45° from broadside. In paper II the same type of element was studied, with the intent to solve three specific problems: the numerical accuracy of the method, how to simplify the manufacturing of the antenna, and the wide-angle scanning performance. For the analysis, a finite-difference time-domain (FDTD) code with periodic conditions (PBFDTD) was used [35]. The model in [34] used a coarse mesh, with only one FDTD-cell to represent a metallic pixel, see Fig. 3.3. This was too few cells to guarantee that the difference between the cost function for two elements is not caused by numerical error. To improve the accuracy of the results the mesh was refined to 4 × 4 FDTD-cells per pixel. The accuracy of these results was evaluated by comparing it with results computed using a mesh with 12 × 12 FDTD-cells per pixel. In Fig. 3.4 the active reflection coefficient is shown

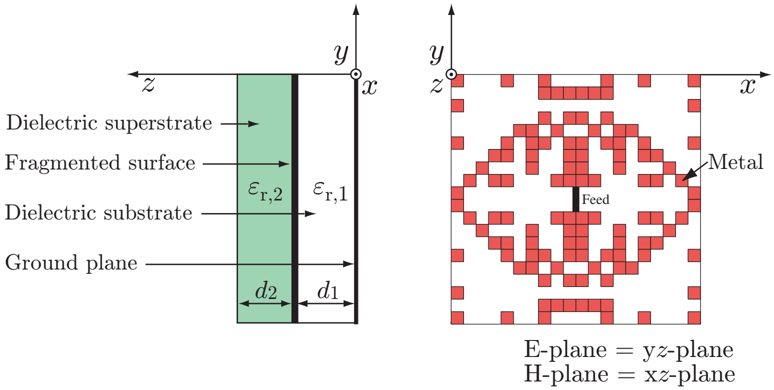

Figure 3.3: Geometry of the fragmented aperture antenna.

for different mesh resolutions, and even if the agreement between the 12×12 and 4×4 results are far from perfect the accuracy was found to be acceptable.

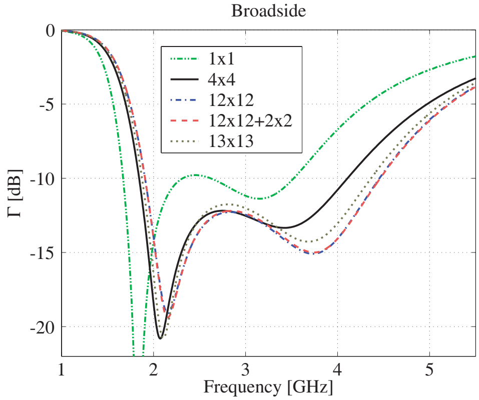

Figure 3.4: Active reflection coefficient for broadside scan for different mesh and critical corner solutions.

A problem with the metallic pattern of these elements were that the diagonal adjoining pixels could cause large current densities that would lead to ohmic losses. To prevent such losses two options were considered. The first option was to add a smaller pixel over the corners and the second was to make the pixels slightly larger so that they are overlapping, see Fig. 3.5. The two options were evaluated and the solutions are shown in Fig. 3.4, where small patch option is denoted $(12 \times 12 + 2 \times 2)$ and the overlapping patch is denoted (13×13). In FDTD a metal edge is slightly larger than the FDTD-cell that the material properties are assigned to, which causes the solutions to converge slowly when the mesh is refined. But if this effect is considered when the model is made, it is possible to compensate to a small degree for this effect. As a consequence the 4×4 pixel model better agrees with the overlapping pixel model due to that they correspond to the same physical pixel width. The conclusion is that the overlapping pixel model is the best choice

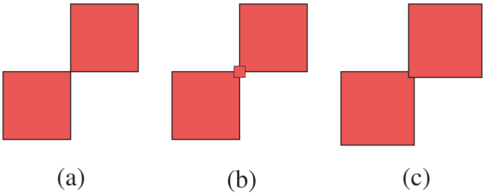

Figure 3.5: (a) Critical diagonal pixel contact (12×12). (b) Small patch covering the critical corner $(12 \times 12 + 2 \times 2)$. (c) overlapping pixels (13×13).

to avoid the ohmic loss problems, since it is a simple solution, and it is also the model that corresponds best to the model that the genetic algorithm evaluates.

In [34] the dielectric constants were continuous variables whereby the final designs could result in non-available dielectric materials. To overcome this problem the algorithm was restricted to a list of commercially available materials. Furthermore, the maximum scan angle $\theta_{\max}$ was changed from 45° to 60°. Two designs were made using this method, one element with a superstrate above the metallic pattern and one element without. The goal was a wide-band wide-scan design. The bandwidth for the resulting elements are good, $\sim 2{:}1$ for $|\Gamma| < -10$ dB, for scan angles within 45° scan from broadside, especially if the low profile of the element is considered, see Fig. 3.6. Not that the performance can be improved if the maximum height of the elements is allowed to increase. However, a more important problem is that in all simulations the feed of the antenna is a discrete point source, and the ideal characteristic impedance of a transmission line connected to this source is usually much higher than the often preferred value of 50 Ω. It is not trivial to design a practical feed for this element without impairing its performance. A similar element with excellent bandwidth and wide-scan range is the dipole with arms that are strongly capacitively coupled between elements, almost physically overlapping [36]. Such an element has basically the same problem with the feed, and it has been suggested by the inventor that it could be fed by two probes through the ground plane with two connectors at the backside. However, dual probe feeds can cause scan blindness [37] and require more complex transmit and receive modules.

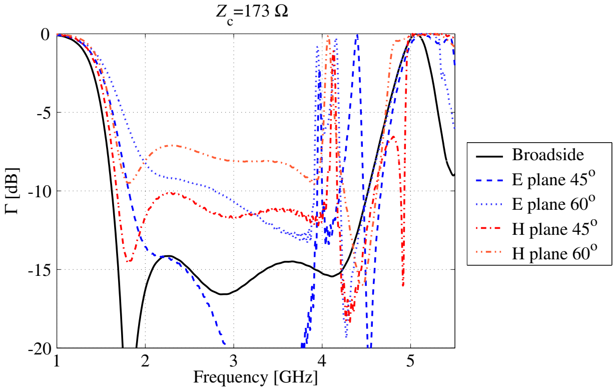

Figure 3.6: Active reflection coefficient for antenna element with a superstrate.

For the fragmented aperture antenna the largest problem is the ground plane. It is basically the ground plane that motivates many of the design choices for this element. In [34] it was shown that the fragmented aperture antenna without a ground plane has performance similar to self-complementary arrays. A self-complementary antenna of infinite extent has no lowest frequency limit and therefore the antenna has an infinite bandwidth [38–41]. When a ground plane is added to the antenna it will introduce a frequency dependence to the active impedance [42]. This phenomena is caused by that the wave emitted from the antenna is reflected by the ground plane and depending on the frequency cause constructive or destructive interference. Since an infinite array only radiates in limited directions the destructive interference can prevent any energy to leave the antenna, which means that the antenna cannot accept any incident power. To improve the bandwidth of elements with a ground plane, both fragmented aperture antennas and the self-complementary antennas use dielectric slabs on top of the antenna and in between the antenna and the ground plane, e.g. this was done in paper II and in [3, 43]. An alternative approach is to use a ferrite loaded ground plane, which improves the bandwidth at the cost of the radiation efficiency. These designs are usually good for antennas that require a low profile, which is practical if the antenna is to be carried by an airplane and the frequencies are $\sim$ 1 GHz and lower. For these frequencies the element spacing is large enough to leave room for the extra connectors required for dual point feeds. However, for this type of elements the element spacing is in terms of wavelength often less than $\lambda/2$ for the highest frequency, which is unacceptable in some applications.

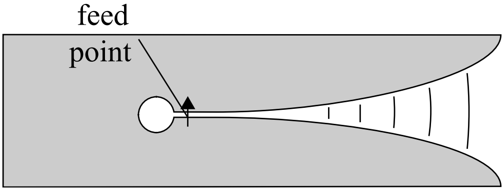

Figure 3.7: A basic tapered-slot element.

3.3 Tapered-slot element

The final class of elements to consider is the tapered-slot element, also known as the flared notch element, or, if the taper is exponential, the Vivaldi element. Tapered-slot elements, which can be used as a single element or in arrays, have been found to have excellent bandwidth [44, 45]. In arrays the elements have been found to have a good wide-scan performance, but they can suffer from resonances and scan blindness effects that limit both bandwidth and scan performance [46–49].

The basic tapered-slot element is a slot line that is gradually widened in one direction and terminated with an open circuit stub in the other, see Fig. 3.7. If the slotline is excited by a potential difference over the slot it creates two waves traveling along the slotline from this point. One of these waves is reflected by the open circuit, ideally without changing its sign. This reflected wave will if it is induced close to the open circuit add constructively with the other wave and gradually leak from the slotline. There are several variants of this element that are all based on the above mentioned interference principle. The elements can either be made from a solid metal sheet or by etching a metallic pattern on a dielectric substrate. Dielectric substrates have the useful property that the feed of the element can be made on the same substrate as the tapered-slot. To shield the feeding network, two substrates are usually bonded together so that there is a tapered-slot pattern on both sides of the element. The two tapered-slot metal layers create a cavity within the substrate, which may cause resonances. To prevent these resonances vias are usually introduced between these layers [50]. The vias reduce the size of the cavities, which in turn increases the corresponding resonance frequencies so that they are moved outside the antennas frequency band. The design of the open circuit stub, feed, and the shape of the tapered-slotline vary much between different designs. Most designs are two dimensional and made from sheets of different materials, but there are also elements that are three dimensional [51–53]. The tapered-slot elements are usually used when the elements are longer than half a wavelength, which is too long for certain applications. The flared dipole [54, 55] and double-mirrored balanced antipodal Vivaldi antennas [56] are close relatives to the tapered-slot. They are shorter and do not need electrical contact between the elements, which is especially practical in dual polarized applications.

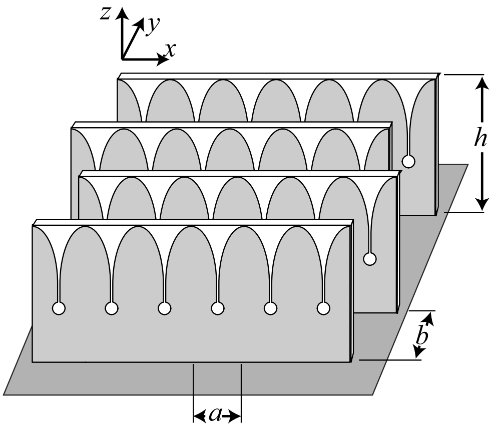

Figure 3.8: Array of tapered-slot elements positioned in a triangular grid.

In this thesis a bilateral tapered-slot fed by a microstrip line is studied. Detailed parameter studies for such elements have been made in [57–59]. The difference between the element presented in this thesis and in previous work is that the present element is designed for large arrays with the elements positioned in equilateral triangular grids, see Fig. 3.8, while previously published designs have been intended for rectangular grids; another difference is that the focus is on wide-angle scan performance rather than bandwidth. In most papers the focus is to maximize the

Band	freq. (GHz)	$\lvert\Gamma\rvert$ (dB)	θ_{max} (Deg)
1	9.0 – 10.0	-12	60°
2	8.5 – 10.5	-10	60°
3	4.5 – 11.5	-8	60°

Table 3.1: Requirements for the tapered-slot design.

ratio $f_{\text{h}}/f_{\text{l}}$, where f_{h} and f_{l} are the highest and lowest frequency limit for the element using some sort of definition of bandwidth (there are many). The highest frequency limit is set by the element spacing, i.e. grating lobes, and therefore the most important factor to minimize is the low frequency limit.

Requirements and mechanical design

Instead of minimizing the low frequency limit the goal has been to match the element as well as possible for a radar band and fairly well for other frequencies. For the waveguide elements the goal was a very wide-scan element with moderate bandwidth. However, due to wishes from our collaboration partner Saab Microwave Systems, the goal was changed, since the expected performance of the frequency selective surface (FSS) required that the antenna would absorb most of the incident power for a certain frequency band. This requirement demands that the antenna is well matched for a much wider frequency band, see Tab. 3.1. Since bandwidth and scan performance are conflicting requirements the maximum scan angle was reduced to 60° for both the E and H planes.

The limitations of the budget for manufacturing the antenna system led to the requirement that the antenna was restricted to a single polarization. However, with no reception of the second polarization the ground plane increases the backscattered field for cross polarized incidence. To reduce this effect, an absorbing layer is positioned on top of the ground plane, wherefore the antenna element needs to be extended from the ground plane by the same length as the absorber is thick. Even though an absorber may reduce the radiation efficiency of the antenna, it is not a problem in the present case. The substrates create a parallel waveguide structure that is below cutoff for the antenna's co-polarization and operational frequencies. However, the absorber will cause losses when guided modes, that otherwise would lead to scan blindnesses, are excited between the substrates. Furthermore, to add extra stability to the array, the space between the elements is filled with a foam material with a dielectric constant close to unity. Finally, a thin glass fibre layer was mounted on top of the foam for mechanical protection.

It is preferable to have as few elements as possible in the antenna. A conflicting requirement, however, is that the antenna has to be free of grating lobes up to a certain frequency, which requires a dense grid. This is important for the performance at large scan angles, and for the radar cross section (RCS). The highest frequency for which the antenna is required to be free of grating lobes is set to

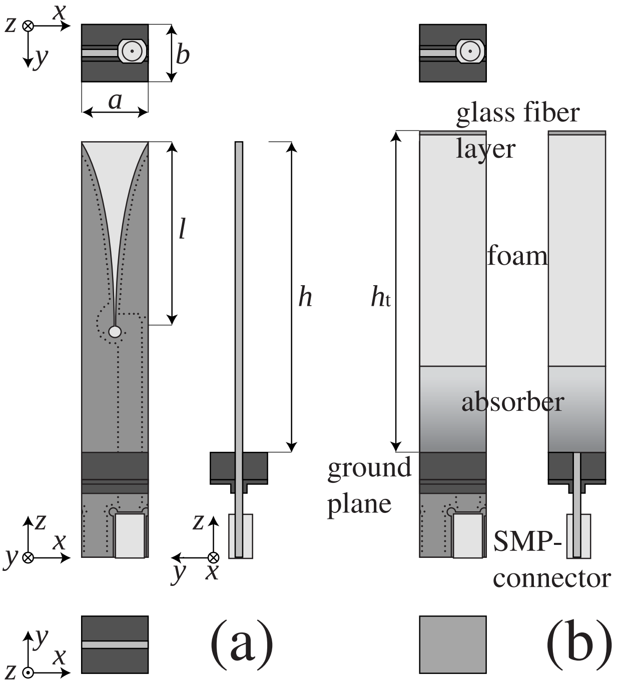

Figure 3.9: Geometry of a unit-cell of the phased array. Figure (a) depicts the antenna element without the absorber, foam and, the glass fiber layer. Figure (b) depicts the antenna element as it is in the phased array. The dimensions for the experimental antenna are $l = 36.4$ mm, $h = 64$ mm, $a = 14.3$ mm, $b = 12.5$ mm and, $h_\mathrm{t} = h + 2.3$ mm. Tapered-slot opening rate $R = 0.06$ mm^{-1} [58].

$f_\mathrm{h} = 12$ GHz. The sparsest grid for a grating lobe free antenna is the equilateral triangular grid also known as the hexagonal grid. The sides of the equilateral triangle are $\lambda_\mathrm{h}/\sqrt{3}$, where λ_h is the wavelength at the grating lobe frequency f_h. Thus $a = \lambda_\mathrm{h}/\sqrt{3} \simeq 14.3$ mm, $b = \lambda_\mathrm{h}/2 = 12.5$ mm, $c = a/2$ in Eq. (2.11).

Electrical design

The electrical design process was divided into three steps. The first step was to create a slotline to stripline transition, the second step was to design the tapered-slot shape, and the third step was to add a stripline impedance transformer. The stripline to slotline transition is a standard transition for this type of element, using a circular short stub for the slotline and a feather shaped open stub for the stripline [57], see Fig. 3.10. Due to manufacturing tolerances the stripline impedance is chosen to 70 Ω. Hence, a stripline impedance transformer is needed

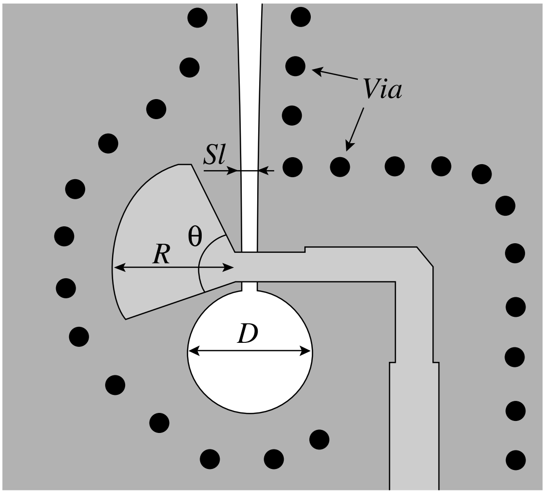

Figure 3.10: Illustration of the stripline to slotline transition. $Sl = 0.3$ mm $R = 2.6$ mm $D = 2.9$ mm $\theta = 90°$.

to get a 50 Ω interface.

The shape of the element is an exponential taper [58], and its most important parameter in this design is its length l. The tapered-slot element works basically as a tapered transmission line transformer. Because of the taper the absolute value of the active reflection coefficient will oscillate as a function of frequency. For large scan angles the local maxima of the active reflection coefficient are difficult to suppress. Therefore, the length of the tapered-slot is tuned so that a local minimum of the active reflection coefficient will be positioned at band 1, see Tab. 3.1. Furthermore, the local minimum is made sufficiently wide to match the width of band 1 for the largest scan angle in the E plane. Note, if the tapered-slot is made longer it will result in a decreased width of the minima of the active reflection coefficient. Furthermore, the maxima and minima will move with scan angle, but the antenna will be better matched for smaller scan angles.

The glass fibre layer that protects the antenna improves the electrical design. The layer acts as a wide-angle impedance matching layer (WAIM) and improves the match for the H plane [60]. The layer works as a susceptance that depends on the scan direction. The susceptance increases with scan angle in the H plane and decreases in the E plane. The dielectric constant determines the angle for which the susceptance is zero in the E plane, which makes it possible to first design an antenna for a maximum scan angle in the E plane. Then a WAIM layer is chosen that does not affect the maximum E-plane scan angle. Finally, the H-plane performance is tuned by alternating the thickness of the layer as well as the height above the element.

The last step in the design process is to add an impedance transformer that changes the impedance interface from 70 Ω to 50 Ω, see Fig. 3.10. To avoid short period oscillations for the active reflection coefficient, the transformer is positioned close to the stripline to slotline transition.

Numerical results

An antenna element was designed using primarily PBFDTD, the same code that was used to analyze the fragmented aperture antenna. The resulting antenna design were well within the requirements set by Saab. In Figure 3.11 the active reflection coefficient is shown for the antenna element without the absorbing layer. In this figure one can observe impedance anomalies for E-plane scan for frequencies above 11 GHz. These anomalies are caused by a scan blindness effect that will be discussed in chapter 5. To verify the design of the element a commercial finite element method code (HFSS) was used and the agreement between the HFFS and PBFDTD-model was considered to be good. In Figure 3.12 the power losses in the antenna are shown for the HFSS model when the absorbing layer is added to the numerical model. With this layer the guided waves are attenuated and the active reflection coefficient is reduced, but at the cost of the radiation efficiency. At these high frequencies the amplitude of the backscattered fields are in general lower when the absorber is included in the array, which was the primary reason why the bandwidth was increased and the absorber was added to the design.

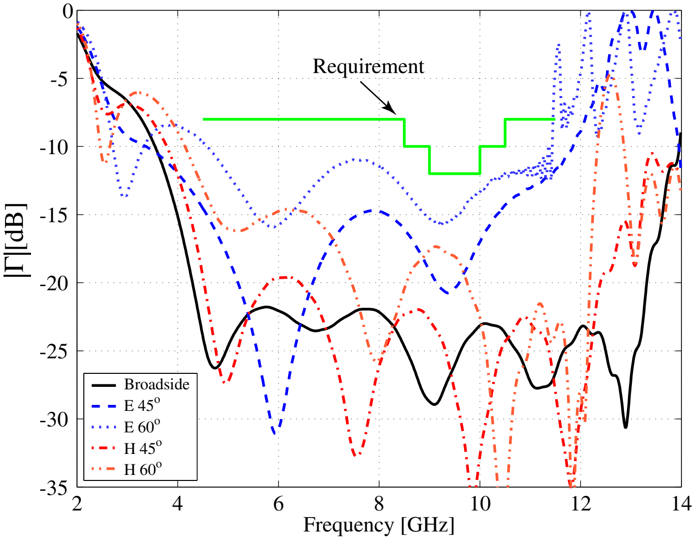

Figure 3.11: Active reflection coefficient for the PBFDTD-model, no absorbing layer.

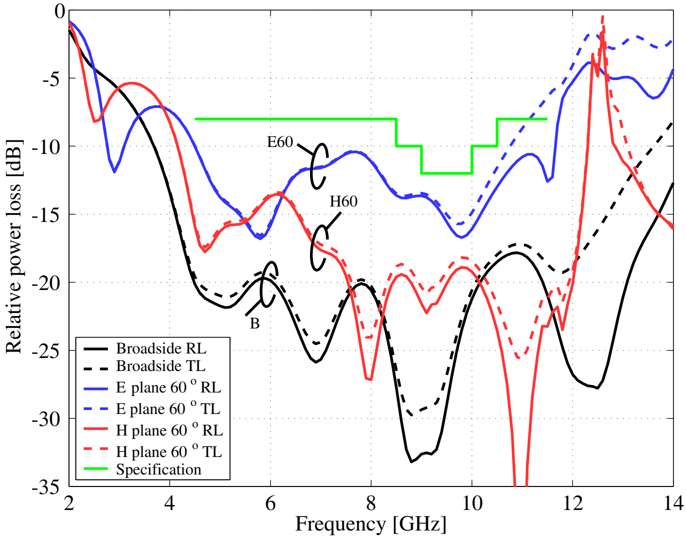

Figure 3.12: Tapered-slot antenna with absorbing layer, return loss (RL) defined as $|\Gamma|^2$, total loss (TL) is defined as $\left(1 - \eta(1 - |\Gamma|^2)\right)$ where η is the radiation efficiency.

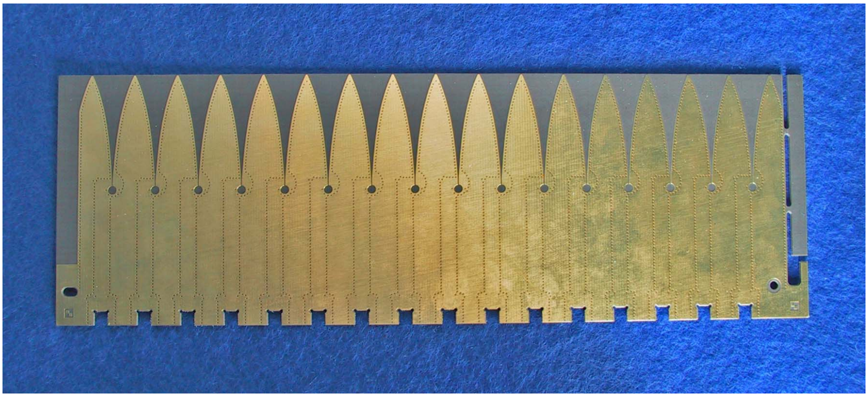

Figure 4.1: A substrate with 16 elements.

Chapter 4

Experimental antenna

A 16 × 16 element experimental array was built to verify the design made with the infinite array approximation. The geometry of the final element design and the dimensions are given in Figs. 3.9–3.10. The antenna consists of 16 rows; one such row is shown in Fig. 4.1. These rows protrude through the ground plane and are fastened on the backside of the ground plane, see Fig. 4.2

In Figure 4.3 the antenna array is shown without the absorbing layer and the protective foam layers. To avoid unnecessary interaction with the edges, the foam layer extends approximately one unit cell outside the elements. Furthermore, the absorbing layer covers both the top and sides of the ground plane, see Fig. 4.4.

A rule of thumb for finite antenna arrays is that the infinite array approximation is valid for the center antenna elements when the array is larger than $5\lambda \times 5\lambda$ [16]. For the experimental antenna this corresponds to 7.5 GHz, but measurements have shown that the agreement is pretty good for frequencies below that limit. The

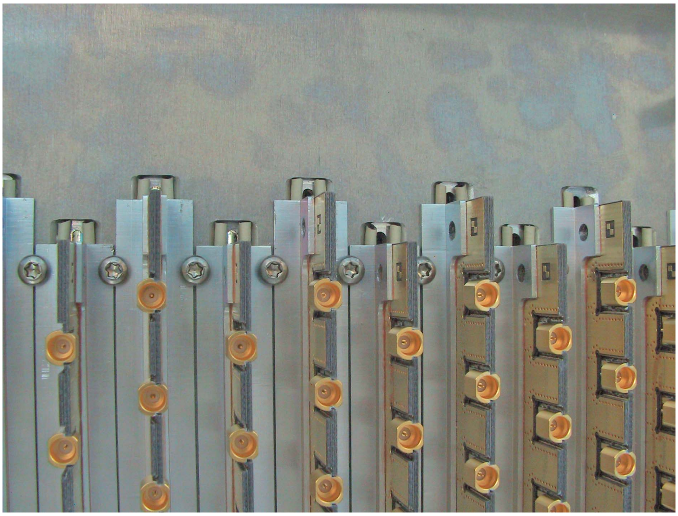

Figure 4.2: Backside of the antenna.

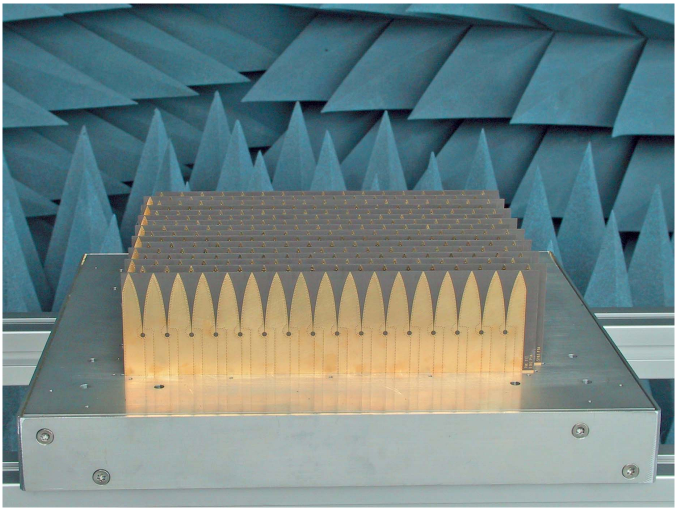

Figure 4.3: Array without the absorbing and protective layers.

experimental array was evaluated by measuring the coupling coefficients and by measuring the embedded element pattern for the central element in the array. The coupling coefficients were used to compute the active reflection coefficient using Eq. (2.3) and (2.9), with the amplitude of all elements set to unity. In Figs. 4.5(a) and 4.5(b), the contours of the active reflection coefficients are shown for the finite

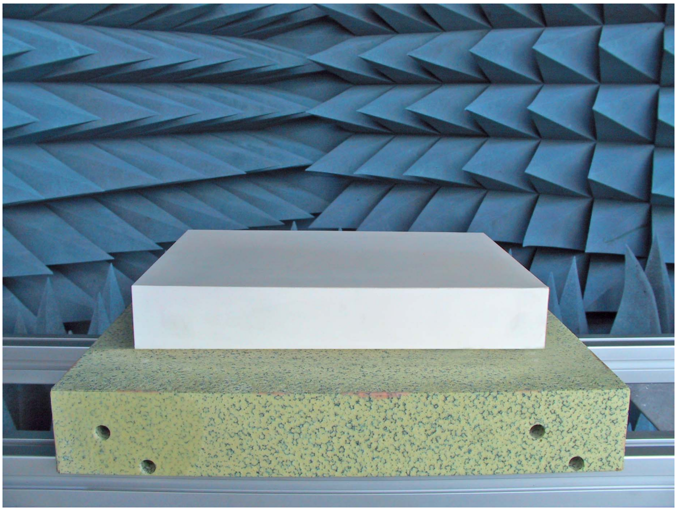

Figure 4.4: Assembled antenna with absorbing and protective layers.

array. The contours are symmetric, which is a good indication that the antenna is well built and that the surrounding elements are fully functional. For comparison, the active reflection coefficient is shown for the infinite array computations in Figs. 4.5(c) and 4.5(d). The largest difference between the measured and computed values are for the H plane, where for large angles the active reflection coefficient is larger than for the infinite array. This is a finite array effect due to a diffracted wave caused by the truncation of the infinite array.

In this case, where the antenna includes losses, the coupling coefficient data is not sufficient to answer whether the antenna radiates well, since it can be well matched due to dissipation in the absorbing layer. Therefore, it is important to verify the antenna by measuring the radiation characteristics. In Figure 4.6 the embedded element patterns are shown for two cut planes, the E plane cut and the H plane cut, for the co- and cross-polarizations. Also shown in these figures are the maximum gain for an infinite array and the embedded gain computed using Eq. (2.34) with the measured active reflection coefficient. Equation (2.34) is valid for the lossless infinite array, but in Fig. 4.6 the radiation efficiency is not equal to 1 for 12.5 GHz.

For 6.5 GHz and 9.5 GHz the agreement between the measured results is fairly good, although for the latter frequency the measured element pattern fluctuates for unknown reasons. These fluctuations could be caused by diffraction from the edges or by the measurement range.

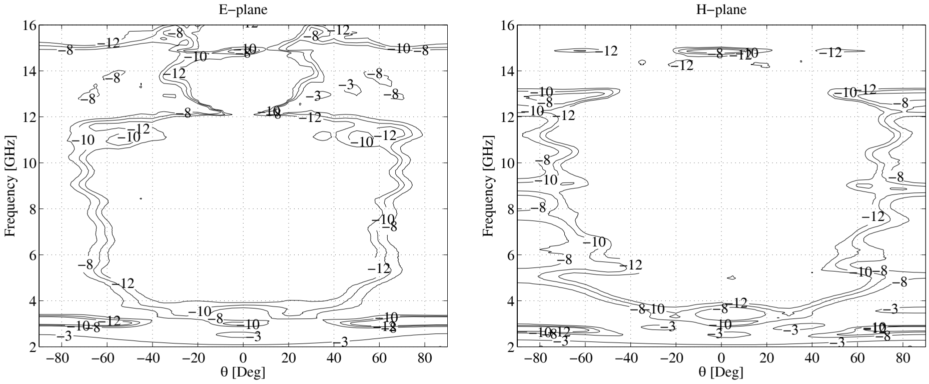

(a) E plane, measurements (b) H plane, measurements

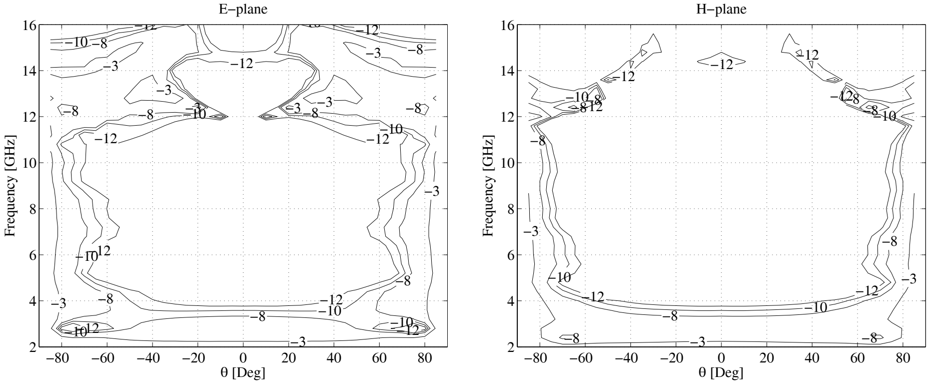

(c) E plane, infinite array computations (d) H plane, infinite array computations

Figure 4.5: Contours of the active reflection coefficient (dB).

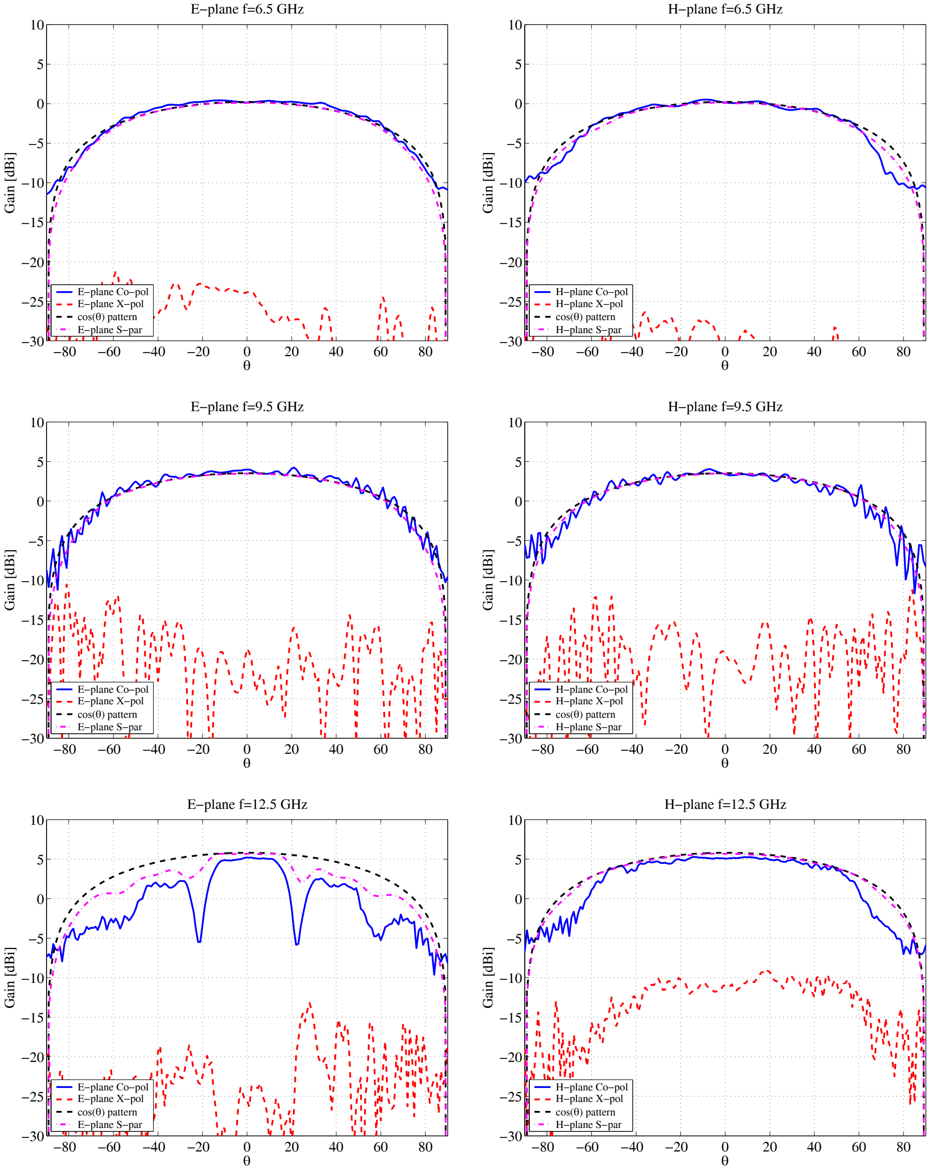

Figure 4.6: Embedded element patterns for the central element.

Chapter 5

Scan blindness

One of the observed effects in the previous chapters is that when scanned in the E plane the tapered-slot antenna is mismatched for frequencies close and above the high frequency limit. This type of impedance mismatch is caused by three types of scan blindness, which are discussed and modeled in papers III-V. Similarly, the fragmented aperture element with a superstrate is also mismatched for large scan angles, which is also caused by a type of scan blindness.

All these scan blindnesses have in common that they depend on the frequency as well as the phase shift between the elements. If the phase shift is changed, so is the frequency for which the scan blindness occurs. These scan blindness effects appear when guided modes are excited in the antenna structure, which occurs when the propagation constant of the guided mode coincides with that of a Floquet mode. The scan blindness condition depends on the array grid and the polarization of the guided mode.

5.1 Dielectric slab on top of a ground plane

The most well known cause of scan blindness is the excitation of a surface wave in a dielectric substrate on top of a ground plane [61–63]. A surface wave is a slow wave that travels along the boundary between two different media. This wave has a phase velocity that is less than the phase velocity of a wave in an unbounded medium with the same electromagnetic properties. In the surrounding media the amplitude of the surface wave decreases exponentially in the direction away from the boundary. Let's consider an example with a dielectric slab on top of a ground plane that is positioned in the xy-plane with the air/dielectric boundary at $z = 0$. In the air region the relation between the wave numbers for the surface wave are

$$\begin{aligned} k^2 &= \beta_x^2 + \beta_y^2 + \beta_z^2 \\ \mathrm{Im}(\beta_z) &> 0 \\ z &\geq 0 \end{aligned} \tag{5.1}$$

which gives

$$\beta_{\mathrm{su}}^2 = k^2 - \beta_z^2 = \beta_x^2 + \beta_y^2 \tag{5.2}$$

where β_{su} is the longitudinal wave number of the surface wave. To compute the transverse wavenumber, β_z, a dispersion relation needs to be solved that depends on the thickness and the electromagnetic properties of the dielectric slab [64,65]. The surface wave couples very strongly to the array when the wavenumber coefficients coincide with the Floquet excitation, e.g.

$$\begin{aligned} \beta_x &= k_{xpq} \\ \beta_y &= k_{ypq} \end{aligned} \tag{5.3}$$

This scan blindness condition is depicted in the grating lobe diagram in Fig. 5.1. The surface wave longitudinal wavenumbers in Eq. (5.2) lie on a circle with a radius $|\beta_{\mathrm{su}}|$, depicted in the figure as a red dot dash circle. The (p=-1,q=-1) Floquet mode is in the figure steered so that it coincides with the surface wave circle, and if the antenna can couple to this surface wave it will cause scan blindness.

It follows from Eq. (5.2) and (5.2) that the radius of the circle depicting the scan blindness condition in the grating lobe diagram in Fig. 5.2 is larger than the visible region circle. This means that the surface wave will cause the antenna to be mismatched before a grating lobe enters visual space, which leads to that an element designer must use smaller element spacing than required by the grating lobe condition.

5.2 Tapered-slot triangular grid scan blindness

In paper IV the scan blindness condition in Eq. 5.3 was used for taped-slot arrays with the elements positioned in triangular grids [49]. In this type of antenna the excited guided wave is a leaky mode that propagates in between the substrates. A leaky mode is a fast wave, and would normally radiate from the aperture. However, when the array is scanned in the E-plane the electric fields of the leaky modes are directed from the substrates, due to the symmetry of the element and excitation, and are therefore odd in the transverse direction to the E plane, see Fig. 5.2. The odd field distribution causes the radiated fields to interfere destructively for E-plane scan directions, and hence the leaky modes will not radiate unless a grating lobe directed from the E plane enters visual space. The leaky mode can be described as a TE-mode with wavenumber β_{lw} in the direction along the substrates and with a phase shift between the substrates of $\phi_y = k_y b = \pi$ in the transverse direction of propagation. The lower frequency limit is set by the element spacing in the E plane, where the leaky mode ceases to propagate for a spacing smaller than $\lambda/2$. For these leaky modes the phase progression coincides with the Floquet modes with index $p = \pm 1, q = n$, in a triangular grid array, where n is any integer.

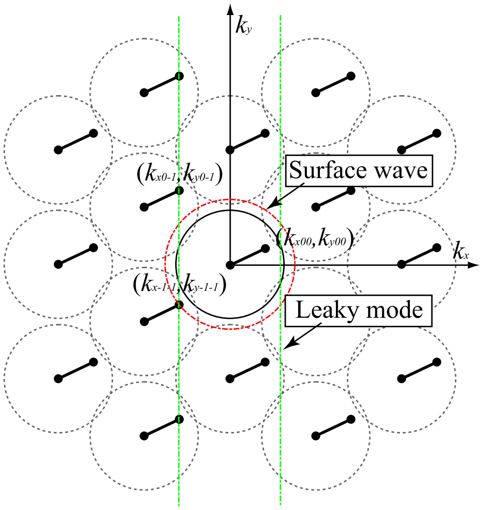
k_y
k_x
$(k_{x0\text{-}1}, k_{y0\text{-}1})$
Surface wave
(k_{x00}, k_{y00})
$(k_{x\text{-}1\text{-}1}, k_{y\text{-}1\text{-}1})$
Leaky mode

Figure 5.1: Grating lobe diagram that shows the longitudinal wavenumbers for a surface wave in a dielectric slab and the longitudinal wavenumbers for the leaky mode that causes scan blindness in the tapered-slot arrays in triangular grids. The scan blindness condition is fulfilled when the longitudinal wave numbers of a Floquet mode coincide with the longitudinal wavenumbers of the guided mode.

This type of scan blindness cannot occur for a rectangular grid tapered-slot array steered in the E plane due to the imposed symmetry of the elements and the rectangular grid. In rectangular grid arrays scanned in the E plane the fields lines must be in the same direction between two substrate regions. However, that is impossible since the symmetry of the elements and the excitation requires that the field lines have opposite directions from the substrates in the transverse direction. If $\beta_{\mathrm{lw}} = k_x$ for the triangular grid array for other scan directions than the E plane, there is no guaranty that scan blindness will occur, since then the leaky mode could theoretically radiate. However, this relaxed conditions often leads to that the active reflection coefficient changes rapidly and the antenna becomes mismatched. The relaxed scan blindness condition can be illustrated in the same way as the surface wave scan blindness condition, see Fig. 5.1. In this figure the Floquet modes with $(p = -1, q = n)$ fulfil the relaxed scan blindness condition when the element spacing in the E plane is larger than $\lambda/2$. At the lowest frequency, the relaxed scan blindness occurs for $\theta_0 = 90°, \phi_0 = 0$ and the scan blindness angle decreases with increasing frequency, see Fig. 5.3. For this guided mode the field intensity is high close to the ground plane and therefore the absorbing layer over the ground plane in the experimental antenna will attenuate the wave, as could be observed by comparing Fig. 3.11 and 3.12. This effect is also shown in Fig. 5.3(b) where the dissipated power in the absorbing layer relative to the incident power applied at the port of the

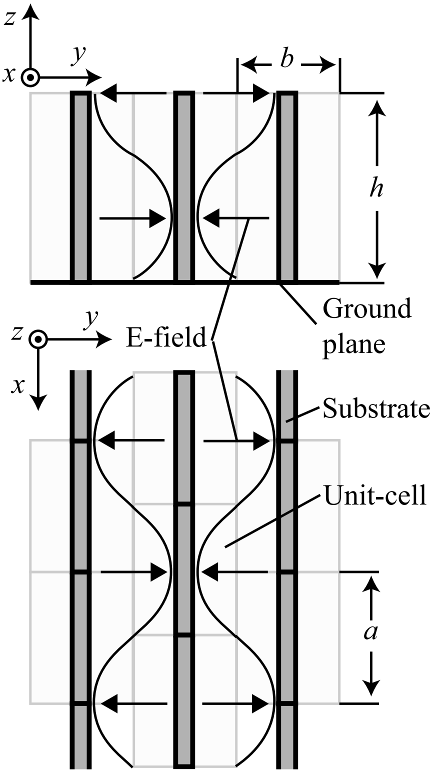

Figure 5.2: Electric field distribution of the leaky mode for the tapered-slot triangular grid scan blindness.

element is shown as a function of the scan angle in the E-plane and the frequency.

5.3 Broadside scan blindnesses

In both rectangular and triangular grid tapered-slot arrays there exist two types of scan blindness that have the opposite frequency behavior to the previously discussed scan blindness. These scan blindnesses occur for the lowest frequency for broadside scan and the scan blindness angle increases with the frequency, see Fig. 5.3. Instead of using the scan blindness condition in Eq. (5.3), to fit a known guided mode to a Floquet mode, a Floquet mode is used to calculate the guided mode. For this type of guided mode the phase progression along the E-plane is arbitrary and can be chosen equal to any Floquet-excitation. The scan blindness condition can be derived from a transmission-line circuit for propagation along the z-axis. The guided modes propagate downwards, as seen from the top of the antenna, and are reflected back

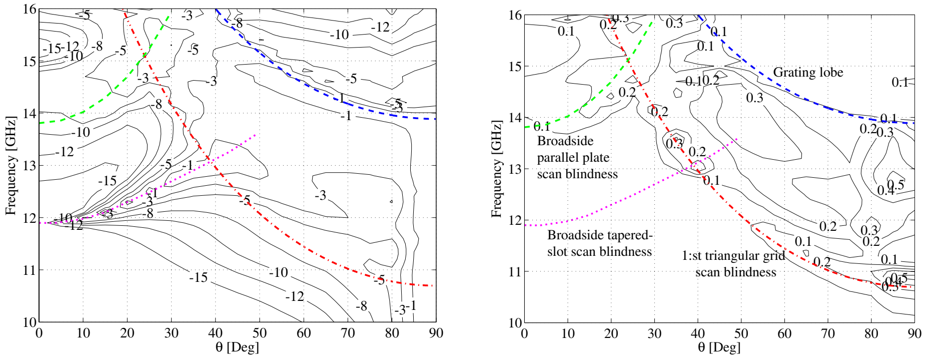

(a) Total losses (dB) (due to mismatch and reduced radiation efficiency)

(b) Dissipated power in the absorbing layer relative to the incident power (-)

Figure 5.3: The three scan blindnesses types that occur for the experimental antenna tapered-slot design when scanned in the E-plane.

either by the ground plane or by the tapered-slot, and the scan blindness occurs when the impedance at the aperture is equal to the Floquet mode wave impedance, see Fig. 5.4. In Figure 5.4 the wave impedance of the mode in the antenna is denoted Z_a and the wave impedance of a Floquet mode is denoted Z_FL. Furthermore, the antenna transmission-line is terminated with an impedance Z_l at the length h from the aperture.

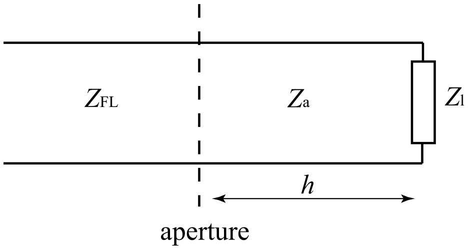

Figure 5.4: Transmission line model used for the broadside parallel plate scan blindness

Broadside parallel plate scan blindness

The most well known of the broad side scan blindness types mentioned above occurs when the spacing between two substrates is larger than $\lambda/2$ [46]. The antenna is modeled as a parallel plate waveguide and a TM$_z$-mode can be supported by this structure. The mode propagates between the parallel plates and is reflected by the ground plane. The resonance condition with appropriate Z_a, Z_FL, and Z_l in Fig. 5.4 above for this scan blindness is

$$\beta_z^\mathrm{a} \tan(\beta_z^\mathrm{a} h) = -\mathrm{j}k_{zpq}. \tag{5.4}$$

Here β_z^a is the wavenumber along the z-axis for the guided mode and h is the height of the substrate, see Figs. 3.9 and 5.4. Equation (5.4) has solutions for the Floquet modes with index $(p = 0, q = \pm 1)$. These Floquet modes are the same for rectangular and triangular grids, since they do not depend on the element spacing along the E-plane. In the experimental antenna the spacing between the substrates is 10.9 mm and the scan blindness occurs for frequencies higher than 13.8 GHz. This is not a problem in the experimental antenna, since the maximum frequency requirement is 11.5 GHz. Note that this scan blindness interacts with the ground plane and the use of an absorbing layer covering the ground plane will dissipate the guided wave. This phenomenon can be seen in Fig. 5.3(b) where the scan blindness condition for the broadside parallel plate scan blindness is shown as a green line.

Broadside tapered-slot shape scan blindness

The last scan blindness depend on the shape of the tapered-slot, and for the element design presented in paper V it limits the upper frequency bound for many scan angles in the E-plane. This scan blindness is not as well studied as the previous two [46, 49], and there is no known analytical model for the guided mode. Like broadside parallel plate scan blindness, the broadside tapered-slot scan blindness is not affected when changing between triangular and rectangular grids, from which it is likely that it also couples to the same Floquet modes as the previous scan blindness. Numerical calculations have shown that the scan blindness can be moved up in frequency if either the H-plane spacing is reduced, the slot is made shorter, the slot is made narrower, or the dielectric constant is decreased. The field intensity of the guided mode is low close to the ground plane, since the fields are reflected by the slot instead of the ground plane. This lower field intensity at the ground plane is the reason that the absorbing layer covering the ground plane has little or no effect on this scan blindness. In Figs. 5.3(a) and 5.3(b) the broadside tapered-slot scan blindness is shown as a pink dotted line, and it is clear in Fig. 5.3(b) that the dissipated power in the absorber is negligible for this scan blindness.

Chapter 6

Edge effects

In Chapter 4 we saw that the measured active reflection coefficient agreed fairly well with the active reflection coefficient for the infinite array. The absolute value of the measured active reflection coefficient usually oscillates around the infinite array result. However, for large scan angles in the H plane the measured active reflection coefficient will oscillate around a mean curve above the active reflection coefficient for the infinite array. Both these effects can be classified as edge effects. An edge effect is basically anything that causes the finite array element results to deviate from the infinite array results.

The edge effects are caused mainly by three factors: 1. the excitation is spatially truncated compared with the Floquet excitation, 2. the geometry close to an edge affects the electrical properties of the elements, 3. unattenuated guided waves are reflected by the edges and create a standing wave pattern over the aperture [66]. These three effects can be hard to distinguish from each other, but all of them must be included in an accurate calculation of the coupling coefficients of the array.

The coupling coefficients can be computed for the infinite array using Fourier series expansion, see Ch. 2.2 and [7, Ch. 4]. By using the coupling coefficients for the infinite array we can effectively model the truncated excitation. This is not the case for the perturbation of the current caused by the edge. To compute the edge perturbation of the currents, the finite array problem needs to be solved. The coupling coefficients can be calculated for the finite array directly if the computational resources are available. However, to analyze large finite arrays one usually require computational recourses such as computer clusters. To simplify the problem one can consider arrays that are finite in only one of the two directions. Then the computational domain is reduced and the effects of a single edge can be isolated if the finite-by-infinite array is large enough [11].

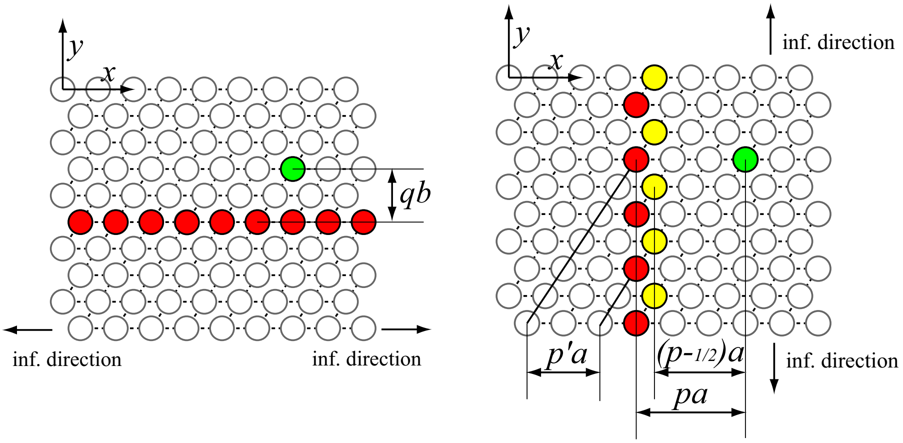

(a) H-plane edge model

(b) E-plane edge model

Figure 6.1: The linear arrays are chosen so that they are parallel to the edge in the finite-by-infinite array.

6.1 Finite-by-infinite arrays

Antennas that are finite in only one direction can be analyzed by using periodic boundaries in the infinite direction, which is equivalent with analyzing an infinite linear array of finite arrays, see Fig. 6.1. The S-parameters computed using periodic boundaries represent the coupling between a single element and an infinite linear array excited with a one dimensional Floquet excitation. The S-parameters can be calculated for the infinite array by calculating the coupling to an element by exciting the same infinite linear array as in the finite array case. In this way Eq. (2.32) can be simplified and the active reflection coefficient needs to be known for fewer scan directions. In paper VII this simplification is used to study the edge effects in a triangular grid tapered-slot array. The S-parameters are computed for infinite arrays and finite-by-infinite arrays for two types of edges. These edges are modeled after the edges in the experimental array in paper V.

We consider an $N \times N$ finite array and will try to model it with infinite $\times$ N or $N \times$ infinite array models. The respective models will be denoted “the E-plane edge model” and “the H-plane edge model” as explained below.

The antenna elements are oriented so that the E-plane coincides with the zx-plane and the H-plane with the yz-plane. The phase difference between two elements along the x-axis, or $\boldsymbol{a_1}$, is $\psi_1 = \psi_x$ and the phase difference between two elements along the other lattice axis $\boldsymbol{a_2}$ can be written $\psi_2 = \frac{1}{2}\psi_x + \psi_y$. Note that the analysis becomes easier if the phase differences are divided into their x and y components, since the edges are parallel to the x- and $y-$axis. Therefore, denote the active reflection coefficient for the infinite array with $S^{\mathrm{FL}}(\psi_x, \psi_y) = S'^{\mathrm{FL}}(\psi_1, \psi_2)$.

The simplest truncation is an edge perpendicular to the H-plane. It is denoted as "the H plane edge" since, when scanning in the H-plane, the beam is scanned towards or away from that edge, see Fig. 6.1(a). The S-parameters for this edge model can be calculated using Eq. (2.32).

$$S_q = \sum_{p=-\infty}^{\infty} S_{m,n(p,q)} \mathrm{e}^{-\mathrm{j}p\psi_{x0}} = \frac{1}{2\pi} \int_{-\pi-\frac{1}{2}\psi_{x0}}^{\pi-\frac{1}{2}\psi_{x0}} S^{\mathrm{FL}}(\psi_{x_0}, \psi_y) \mathrm{e}^{\mathrm{j}q\psi_y} \, \mathrm{d}\psi_y, \tag{6.1}$$

where $\psi_{x_0} = ka \sin\theta_0 \cos\phi_0$ is the phase shift of the excitation along the x-axis.

The other edge is "the E plane edge", when the array is truncated perpendicular to the E-plane, see Fig. 6.1(b). This edge is more difficult to analyze, since the elements are shifted half an element spacing every other element row along the edge. For this edge, two linear arrays are needed to calculate the S-parameters for the corresponding finite-by-infinite array. Along the y-axis the array is excited with a phase shift $\psi_{y_0} = kb \sin\theta_0 \sin\phi_0$. Then, the S-parameters for the first linear array with separation distance pa to the element are

$$S_p = \sum_{p'=-\infty}^{\infty} S_{m,n(p+p',-2p')} \mathrm{e}^{\mathrm{j}2p'\psi_{y0}} = \frac{1}{4\pi} \int_{-\pi}^{\pi} \mathrm{e}^{\mathrm{j}p\psi_x} \left(S^{\mathrm{FL}}(\psi_x, \psi_{y_0}) + S^{\mathrm{FL}}(\psi_x, \psi_{y_0}+\pi) \right) \mathrm{d}\psi_x, \tag{6.2}$$

and the S-parameters for the second array with the separation distance $(p + 1/2)a$ to the element are

$$S_{p+\frac{1}{2}} = \sum_{p'=-\infty}^{\infty} S_{m,n(p+p',-2p'+1)} \mathrm{e}^{\mathrm{j}(2p'-1)\psi_{y0}} = \frac{1}{4\pi} \int_{-\pi}^{\pi} \mathrm{e}^{\mathrm{j}\left(p+\frac{1}{2}\right)\psi_x} \left\{ S^{\mathrm{FL}}(\psi_x, \psi_{y_0}) - S^{\mathrm{FL}}(\psi_x, \psi_{y_0}+\pi) \right\} \mathrm{d}\psi_x. \tag{6.3}$$

The S-parameters were computed numerically for the two edge models for the infinite array and the finite-by-infinite array, with the phase shift along the common infinite direction set to zero. The agrement between the finite and infinite array results is good for elements far from the edge, and poor for elements close to the edge, see Fig. 6.2.

To evaluate the finite and the infinite array S-parameters, the active reflection coefficient can be calculated using Eq. (2.3). The excitation is chosen to be uniform in amplitude with a linear phase shift ϕ between the elements in the finite direction. In the infinite array the excitation was truncated to the corresponding elements in the finite array. In Fig. 6.3 we display the active reflection coefficients computed for four cases, namely: the truncated excitation of the infinite array, the infinite array with Floquet excitation, the finite array, and a combined solution to be discussed later. As expected, the agrement between the different cases is best for elements far

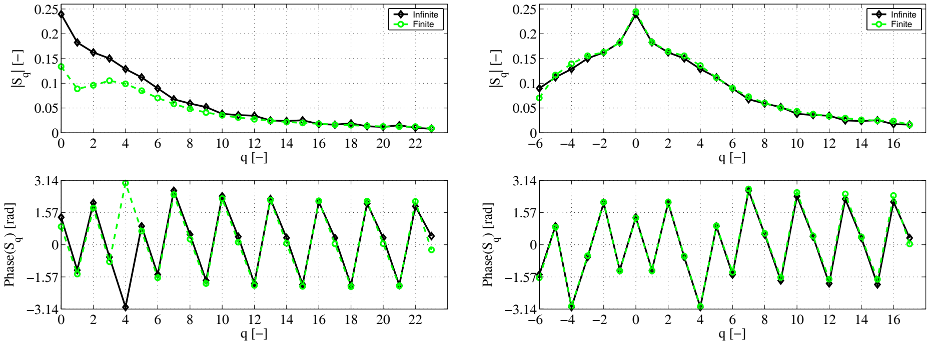

(a) element 1 (b) element 7

Figure 6.2: The scattering parameters for the H-plane edge model, f = 8 GHz. The finite array consists of 24 elements.

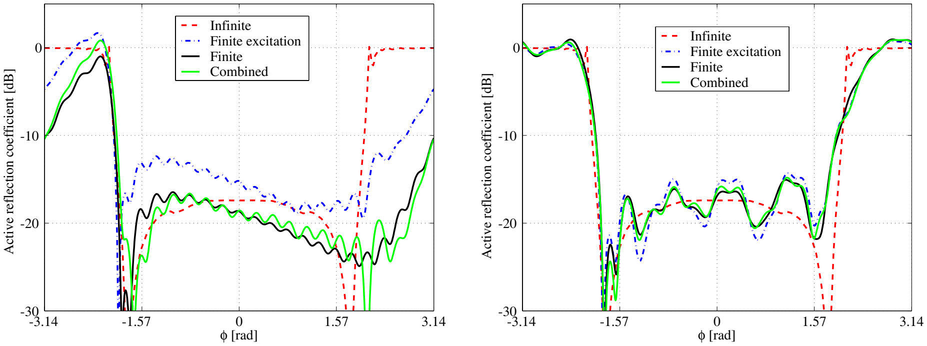

(a) element 1 (b) element 7

Figure 6.3: Active reflection coefficient as a function of phase shift along the y-axis, $\phi = kb \sin \theta$, b = 12.4 mm, f = 8 GHz. The finite array consists of 24 elements. The active reflection coefficient were computed using four methods, namely: the infinite array with Floquet excitation (Infinite), the truncated excitation of the infinite array (Finite excitation), the finite array (Finite), and a combined solution (Combined).

from the edges. Furthermore, the active reflection coefficient varies similarly for the finite array and the truncated infinite array, the local maxima and minima in Fig. 6.3 are basically located at the same phase shift. These oscillations in the truncated array results are caused by the missing contributions from the elements that are not excited or not present. The small oscillations in the amplitude are caused by the edge far from the element, and larger oscillations with a longer period are caused by the closest edge.

The currents are perturbed by the edges of the array, which causes the difference between the finite and finitely excited infinite array. Part of this perturbation can be added to the infinite array result, thereby making it possible to accurately calculate the active reflection coefficient for an arbitrary sized array. If the finite array is sufficiently large, the edge elements will not be affected by the opposite edge and the finite array S-parameters could be combined with the infinite array S-parameters. This is done by using the finite array S-parameters for coupling from elements close to an edge and the infinite array S-parameters for coupling from elements farther away from the edge. This method seems to work pretty well and reduces the largest discrepancies between the finite array and finitely excited infinite array, see Fig. 6.3.

6.2 Infinite array data

To calculate the S-parameters one must know the active reflection coefficient for all scan directions. Due to the periodicity of the Floquet excitation, the scan directions can be limited to the phase shifts along the primitive vectors $-\pi < \psi_1 < \pi$ and $-\pi < \psi_2 < \pi$, and if these parameters are sampled close enough the required values to calculate the integral in Eq. (2.32) can be found by interpolation. Some of these phase shifts correspond to invisible space, when no beam radiates from the antenna. These scan directions cannot be computed directly using FDTD-codes based on unit-cell approaches with time shifts between the boundaries, i.e. a time-domain version of the Floquet theorem [48, 67]. In paper VI a method is presented that describes how to calculate arbitrary phase shifts for an infinite array using a numerical code that is restricted to phase shifts that correspond to visible space.

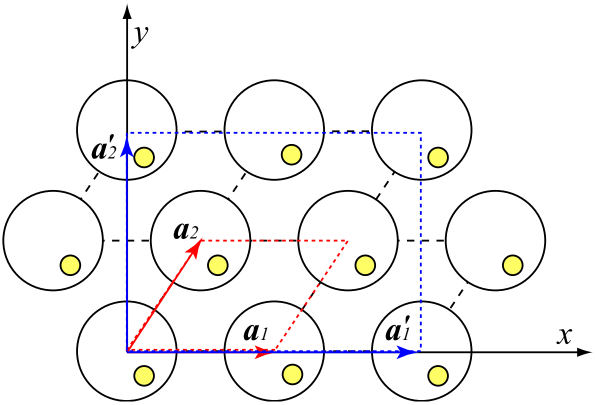

Figure 6.4: The computational domain of the unit cell compared with the larger computational domain used to compute additional phase shifts.

The basic idea is that a computational domain, with a phase shift between its boundaries, that contain more than one element can be used to calculate several different linear phase shifts for the infinite array. This can be done if the S-parameters are calculated for the elements in the computational domain and then weighted together to calculate the active reflection coefficient. This method was used to calculate the active reflection coefficient, needed for the calculation of the S-parameters for the infinite tapered-slot array. Four elements were included in the computational domain, to be able to span the required phase shift space and to keep the triangular grid, see Fig. 6.4. The computational domain containing four elements is a new unit cell of a rectangular grid, with the primitive vectors $\boldsymbol{a'_1} = 2a\hat{\boldsymbol{x}}$ and $\boldsymbol{a'_2} = 2b\hat{\boldsymbol{y}}$. The phase shifts between the boundaries of this computational domain are ψ'_1 and ψ'_2, and they correspond to four different phase shifts for the original unit cell defined by $\boldsymbol{a_1}$ and $\boldsymbol{a_2}$. In this case the relations between the four phase shifts for the original unit cell and the new unit cell are given by $\psi_x = \psi'_1/2 + \pi m$ and $\psi_y = \psi'_2/2 + \pi n$, where m and n are arbitrary integers. This means that the phase shifts spanned with the standard method, i.e. the phase shifts enclosed by the visible space circle, are translated π/a along the k_x-axis and π/b along the k_y-axis in the grating lobe diagram. The translated visual space circles are the same as the grating lobe circles for the larger unit cell, see Fig. 6.5.

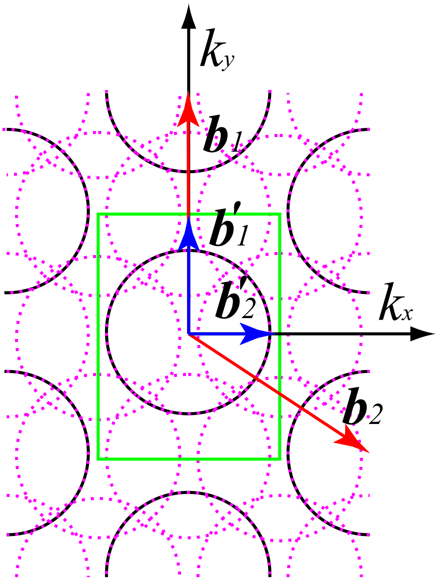

Figure 6.5: The green square represent the phase shifts that need to be spanned to compute the scattering parameters for the infinite array and the purple dashed circles represent the phase shifts that can be spanned by using the larger computational domain.

Given that the grating lobe circles of the larger computational domain cover all the possible phase shifts, it is possible to compute all phase shifts for the infinite array. However, for low frequencies there will be phase shifts that are in between these grating lobe circles. In Figure 6.6(a) the active reflection coefficient in the E-plane, for the tapered-slot element in paper VII, is shown as a function of frequency and phase shift. The white areas in this figure are the phase shifts that were outside the grating lobe circles and for which the active reflection coefficient is unknown. To solve this problem one can either expand the computational domain or use a numerical code that is capable of arbitrary phase shifts.

There are FDTD-codes that use fix phase shifts between the boundaries [68]. A fix phase shift between the boundaries means that the scan direction changes with frequency. This is perfect when calculating S-parameters, but cumbersome when one wants to design an array element for a maximum scan angle. In Figure 6.6(b) a code TFDTD, described in [69] with the periodic boundaries described in [70], was used to calculate the active reflection coefficient for the same case as in Fig. 6.6(a). Due to limited access, this code was primarily used for verification of the method described in paper VI. However, in paper VII the active reflection coefficient computed using TFDTD was used for the frequencies and phase shifts not spanned by the enlarged computational domain. The results computed using PBFDTD and TFDTD agree very well, most of the discrepancies between the results shown in Fig. 6.6 are due to interpolation errors caused by there being fewer scan directions used for the TFDTD computations.

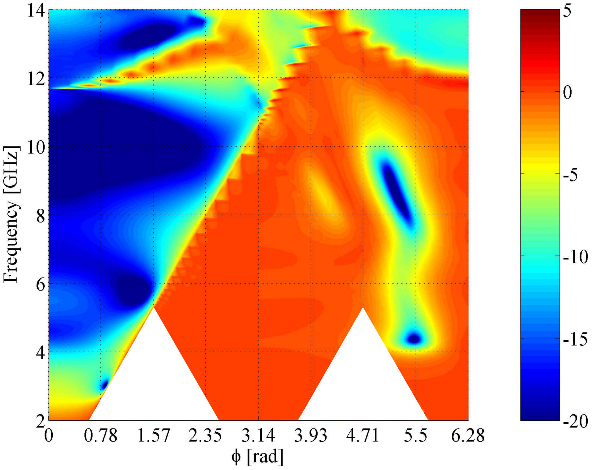

(a) Time shift boundaries with four elements in the computational domain. (PBFDTD + extended domain algorithm)

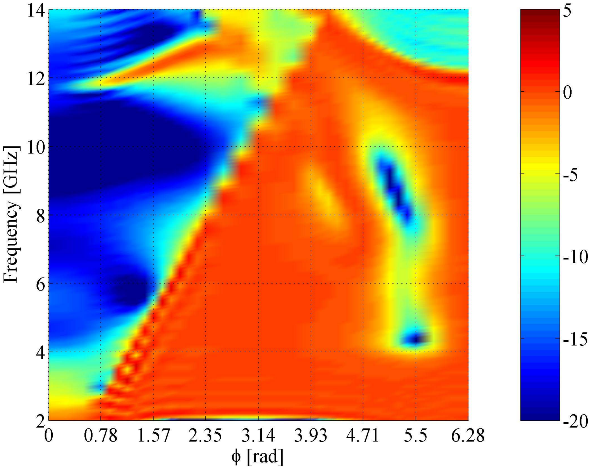

(b) Phase shift boundaries. (TFDTD)

Figure 6.6: Active reflection coefficient as a function of frequency and phase shift along the x-axis, $\phi = ka \sin\theta$, $a = 14.1$ mm.

Chapter 7

Conclusions

The subject of the thesis is planar phased arrays capable of wide-angle scanning. Part of the thesis work was to design an antenna element for a phased array radar antenna. To find suitable candidates for the application a literature study was made in our report [23] to identify antenna elements with good wide-angle performance.

At the beginning of this thesis work the goal for the radar antenna to be designed was an element capable of scanning 75° from the aperture normal. The antenna was supposed to be a planar array antenna that was easy to manufacture and which consisted of as few elements as possible. To simplify the analysis, the array was assumed to be large enough to be modeled as an infinite structure. The requested bandwidth of the antenna was moderate, in the order of half an octave, and it was supposed to be well matched with an active reflection coefficient that was less than -10 dB for all scan angles out to 75° from broadside.

Starting from these requirements, the wide-angle scanning limits were studied for waveguide elements in a ground plane. The elements were matched conceptually using a simple circuit model, in which parameters were chosen by minimizing the reflected power for the intended scan range. It was found with this matching method that the waveguide elements were capable of large scanning angles but required additional scan improving techniques to be able to fulfill the requirement for even a single frequency.

These difficult requirements was changed during the thesis due to the expected performance of the frequency selective surface (FSS) that will cover the antenna. A well matched antenna works as an absorber for an incident plane wave. Therefore, a wide-band antenna was preferred to reduce the radar cross section for the frequency bands for which the FSS is transparent. However, wide-angle scan performance is related to the bandwidth of the antenna and if one requirement is increased the other needs to be decreased. The new requirements were for a single polarized element capable of a 2.5:1 bandwidth for scan angles out to 60° from broadside.

An element that could potentially fulfill these requirements was the fragmented aperture element. The fragmented aperture element is a novel design and it was considered as a backup element in case the other option, the tapered-slot element, did not work out. A couple of practical problems related to building and analyzing fragmented aperture elements were considered and solved. The fragmented aperture element still has some unsolved deign problems; one is the design of a practical feed.

The element that was chosen for the radar antenna was the tapered-slot element. This element has two main advantages: it is easy to fabricate and it has excellent broadband qualities. The idea was that part of the broadband performance could be traded in the design to achieve a better scan performance. To improve the mechanical stability of the array, the elements are encapsuled by a foam layer that is in turn covered by a glass fibre layer. The glass fibre layer acts both as a protection and as a wide impedance matching layer that improves the performance for the H-plane scan directions. The final design was an element that fulfilled the requirements and incorporated an absorbing layer covering the ground plane, to reduce the radar cross section for the antenna's cross polarization.

The tapered-slot element design was the basis for an experimental antenna built by Saab Microwave Systems. This antenna proved to agree well with the numerical calculations, but also gave ideas for further studies. The active reflection coefficient for the H-plane scan direction is worse for the central elements in the experimental array than in the infinite array calculations. This is shown to result from the truncation of the infinite array, i.e. an edge effect.

Phased arrays often suffer from an effect called scan blindness. This effect, which impairs the performance, is caused by a guided wave in the array structure. In the experimental antenna design, there occur three types of scan blindnesses. One of these scan blindnesses occurs only for triangular grid tapered-slot elements and cannot be excited in a rectangular grid. This scan blindness sets the maximum element spacing and therefore reduces the benefit of the otherwise optimal equilateral triangular grid. The other scan blindnesses occur for the same frequencies for triangular and rectangular grids and appears first in frequency for broadside scan. The most problematic of these broadside scan blindnesses depends on the shape of the tapered-slot, and unlike the two other scan blindnesses there is today no analytical expression for the scan blindness condition. It is a challenge to find such an expression, but it would be a useful tool for an engineer when designing this type of element.

An infinite array element behaves similarly to an element within a large array. The difference between the infinite array solution and the finite array solution is usually referred to as edge effects. In this thesis edge effects for tapered-slot in triangular grids were considered. The edge effects were studied by comparing the scattering parameters for finite-by-infinite arrays with those for infinite arrays. The active reflection coefficient for a finite excitation was calculated for these two cases and showed good agreement for the central elements. The thesis ends with the description of a method that was developed for the use of finite difference time domain codes with time shift boundaries to calculate active reflection coefficients for scan directions in invisible space. This method was used to compute the raw data required to calculate the scattering parameters.

Chapter 8

Summary of papers

8.1 Paper I

Rectangular waveguide elements in infinite planar arrays are analyzed with respect to wide-angle scanning, and results for three types of waveguide apertures are presented. The goal was to find a wide-angle scanning array element with moderate bandwidth that can excite two polarizations. The dual polarization requirement leads to the cross section of the waveguides being either circular or square shaped. Dual polarization elements can have problems due to coupling between the two polarizations. Therefore, a single polarized element was chosen as a reference. A goal was to be capable of scanning out to 75° from broadside. For such a large scan angle, a small element spacing is required to avoid the appearance of grating lobes, which requires that the waveguides are filled with a dielectric material to reduce the size of the waveguide cross section.

The elements were evaluated by computing the average reflected power over the scan range. Before the elements were matched, the waveguide with the largest cross section was the best element in terms of the average reflected power. The elements were then matched using a simple matching scheme which minimized the average reflected power. After the matching procedure, the waveguide with the smallest cross section achieved the best result but was similar to the single polarized waveguide. The reason why the large waveguide could not be as well matched was that when the element was steered out in the diagonal plane a large part of the incident power was reflected back in the orthogonal polarization.

8.2 Paper II

Fragmented patch elements for infinite planar arrays are studied in this paper. The shape of this element is obtained by using a genetic algorithm to minimize the average reflected power over a frequency band for three scan directions. The elements consist of small metal pixels and the optimization algorithm chooses the pattern of these pixels. Like for an idealized dipole the element is fed in the middle with a point source. At the time of the paper these elements were a new design and several issues needed to be resolved to improve the designs and to simplify the manufacturing.

Three improvements were addressed in this paper. First, the new designs were done with 4×4 FDTD-cells per pixel, to describe the geometry, instead of a single FDTD-cell. Furthermore, the 4×4-model was evaluated by comparing the results with results for grids with a 12×12 resolution. The second item that was addressed was the electrical contact between corners of two adjacent pixels. To avoid problems during manufacturing with reduced electrical contact, two solutions were proposed and evaluated. The first solution was to put a small patch over the problematic corners. The results computed using this method were identical to the results without the small patch, which shows that this is a good practical solution to avoid the reduction of electrical contact across corners. The second solution is to make the metal pixel slightly larger so that a small overlap is created. Since metal edges are effectively slightly wider than the grid in an FDTD-model, the overlapping pixel model agree better with the 4×4 optimization model than the corner patch model. The last addressed item was a wide-angle design, in which a thin array element was designed for scan angles out to 60° from broadside scan. Two designs were considered, one with a dielectric superstrate on top of the metallic pattern and one without.

8.3 Paper III

In this paper we studied the effect of an absorbing layer covering the ground plane in an array of tapered-slot elements. The tapered-slot elements are configured in a triangular grid and designed for a radar application. To reduce the radar cross section of the polarization that is orthogonal to the antenna element, an absorber is positioned above the ground plane. The absorbing layer does not affect the antenna performance much, since fields with the same polarization as the antenna cannot reach the absorbing layer. The antenna structure works as a parallel plate waveguide structure that is under cutoff for these waves. However, there is a scan blindness effect in this array caused by a guided mode that is excited in between the elements. The absorbing layer will attenuate the guided mode that causes the scan blindness and the antennas radiation efficiency is reduced instead of becoming mismatched. An additional scan blindness is discussed, which is not affected by the absorbing layer; in this thesis it is denoted as the broadside tapered-slot scan blindness. This scan blindness is incorrectly identified in paper III as the scan blindness presented in [46], which still occurs for this antenna but for higher frequencies. The scan blindness in this paper is very similar, but unlike the scan blindness in [46] it depends on the shape of the tapered-slot. Parts of the results in this paper are also published in paper V.

8.4 Paper IV

This paper describes a scan blindness that exists in triangular grid tapered-slot arrays. A simple model for the scan blindness is presented and the model is evaluated. This scan blindness is important because it will for some designs set the maximum frequency limit for the antenna. The maximum unit cell size is 15% larger for triangular grids than for rectangular grids. However, the larger unit cell cannot be utilized completely due to this scan blindness.

The scan blindness depends primarily on two element parameters, the height of the element and the width of the tapered-slot element along the E-plane. The scan blindness occurs when the width is longer than half a wavelength and the scan blindness angles decreases when the frequency increases. If the element height above the ground plane is increased, the scan blindness angle occurs for a lower frequency. In the limit when the height of the element goes to infinity the scan blindness occurs for the same angle and frequency as the grating lobe in a rectangular grid with the same element spacing.

8.5 Paper V

This paper describes a design of a triangular grid tapered-slot array. The main focus was on the design of an array element suitable for radar applications. This element needs to be well matched for a wide frequency band but also to have a low radar cross section for the antenna's orthogonal polarization. The wide-scan performance is met due to careful modeling of the tapered-slot shape and a wide-angle impedance matching layer. To reduce the radar cross section an absorbing layer is positioned above the ground plane. This layer interferes little with the antennas performance with the exception that it reduces the scan blindness effects that exist for this design. This antenna element has three scan blindness effects, of which two are affected by the absorbing layer.

An experimental antenna consisting of 16×16 elements was built and evaluated. The measured active reflection coefficient for the center element was compared with the active reflection coefficient for an element in the infinite array. The agreement was good for broadside scan as well as E-plane scan. The results for the H-plane scan deviated more than expected from the infinite array result. This has been shown to be a finite array effect and it does not occur from incorrect manufacturing of the antenna.

8.6 Paper VI

In this paper a method is presented that describes how to calculate arbitrary phase shifts for an infinite array using a numerical code that is restricted to phase shifts that correspond to visible space. This is a problem with finite difference time domain codes that use time shifts between the periodic boundaries.

The basic idea is that a computational domain, with a phase shift between its boundaries, and containing more than one element, can be used to calculate several different linear phase shifts for the infinite array. This can be done if the S-parameters are calculated for the elements in the computational domain and then weighted together to calculate the active reflection coefficient.

Two numerical examples are given in this paper. In the first example a computational domain with three dipole elements is used to calculate the three different linear phase shifts for the infinite array in a single run. The second example compares the results computed using the method with results from another numerical code.

8.7 Paper VII

In this paper the edge effects in tapered-slot arrays are studied and modeled using coupling coefficients. The arrays were chosen to be infinite in one direction and finite in one direction, since this reduces the size of the problem and the number of edges in the array. S-parameters for the finite-by-infinite arrays are compared with S-parameters for the infinite array for two types of edges. The edge shape was chosen to be the same as in the experimental antenna in paper V. These edges are parallel to either the E plane or the H plane.

It is shown how the S-parameters change with element position. The active reflection coefficients are computed using these S-parameters for the finite array and the infinite array by using a truncated excitation. The active reflection coefficient for these two cases is very similar but differ from the infinite array that is uniformly excited. It is therefore concluded that the dominant cause of the edge effects is the truncated excitation of the array. The difference between the coupling coefficients for the finite array and the infinite array is more prominent close to the edges. This is a secondary effect caused by the currents being perturbed by the finite array edge.

Bibliography

[1] A. Balanis, *Antenna theory*, 3rd ed. Wiley-Interscience, New York, 2005.

[2] P. Patel, D. Kant, E. Wal, and A. van Ardene, "Phased array antennas demonstrator as a radio telescope - embrace," *Antennas and Propagation Society International Symposium, 2008. AP-S 2008. IEEE*, pp. 1–4, July 2008.

[3] S. Hay, J. O'Sullivan, J. Kot, C. Granet, A. Grancea, A. Forsyth, and D. Hayman, "Focal plane array development for ASKAP (Australian SKA pathfinder)," *Antennas and Propagation, 2007. EuCAP 2007. The Second European Conference on*, pp. 1–5, Nov. 2007.

[4] N. Amitay, V. Galindo, and C. P. Wu, *Theory and analysis of phased array antennas.* Wiley-Interscience, New York, 1972.

[5] R. J. Mailloux, *Phased array antenna handbook.* Artech House, Boston, 1994.

[6] R. C. Hansen, *Phased array antennas.* Wiley-Interscience, New York, 1998.

[7] A. K. Bhattacharyya, *Phased Array Antennas.* Wiley-Interscience, New York, 2006.

[8] A. Ishimaru, R. Coe, G. Miller, and W. Geren, "Finite periodic structure approach to large scanning array problems," *Antennas and Propagation, IEEE Transactions on*, vol. 33, no. 11, pp. 1213–1220, Nov 1985.

[9] A. Skrivervik and J. Mosig, "Analysis of finite phase arrays of microstrip patches," *Antennas and Propagation, IEEE Transactions on*, vol. 41, no. 8, pp. 1105–1114, Aug 1993.

[10] A. Neto, S. Maci, G. Vecchi, and M. Sabbadini, "A truncated Floquet wave diffraction method for the full wave analysis of large phased arrays. I. Basic principles and 2-D cases," *Antennas and Propagation, IEEE Transactions on*, vol. 48, no. 4, pp. 594–600, Apr 2000.

[11] C. Craeye, A. Tijhuis, and D. Schaubert, "An efficient MoM formulation for finite-by-infinite arrays of two-dimensional antennas arranged in a three-dimensional structure," *Antennas and Propagation, IEEE Transactions on*, vol. 52, no. 1, pp. 271–282, Jan. 2004.

[12] W. B. Lu, T. J. Cui, Z. G. Qian, X. X. Yin, and W. Hong, "Accurate analysis of large-scale periodic structures using an efficient sub-entire-domain basis function method," *Antennas and Propagation, IEEE Transactions on*, vol. 52, no. 11, pp. 3078–3085, Nov. 2004.

[13] D. J. Beckers, S. J. L. van Eijndhoven, A. A. F. van de Ven, P.-P. Borsboom, and A. G. Tijhuis, "Eigencurrent analysis of resonant behavior in finite antenna arrays," *Antennas and Propagation, IEEE Transactions on*, vol. 54, no. 6, pp. 2821 – 2829, June 2006.

[14] R. Maaskant, R. Mittra, and A. Tijhuis, "Application of trapezoidal-shaped characteristic basis functions to arrays of electrically interconnected antenna elements," Sept. 2007, pp. 567–571.

[15] ——, "Fast analysis of large antenna arrays using the characteristic basis function method and the adaptive cross approximation algorithm," *Antennas and Propagation, IEEE Transactions on*, vol. 56, no. 11, pp. 3440–3451, Nov. 2008.

[16] H. Holter and H. Steyskal, "On the size requirement for finite phased-array models," *Antennas and Propagation, IEEE Transactions on*, vol. 50, no. 6, June 2002.

[17] W. Yu, X. Yang, Y. Liu, L. ching Ma, T. Sul, N.-T. Huang, R. Mittral, R. Maaskane, Y. Lu, Q. Che, R. Lu, and Z. Su, "A new direction in computational electromagnetics: Solving large problems using the parallel FDTD on the BlueGene/L supercomputer providing teraflop-level performance," *Antennas and Propagation Magazine, IEEE*, vol. 50, no. 2, pp. 26–44, April 2008.

[18] G. Paraschos, R. Kindt, D. Schaubert, and M. Vouvakis, "Radiation and coupling studies of finite-size dual polarized Vivaldi arrays using a domain decomposition FEM," *Antennas and Propagation Society International Symposium, 2008. AP-S 2008. IEEE*, pp. 1–4, July 2008.

[19] J. Jian-Ming and R. J. Douglas, *Finite element analysis of antennas and arrays.* IEEE Press, New York, 2008, ch. 11.

[20] "IEEE standard definitions of terms for antennas." *IEEE Std 145-1993*, Jun 1993.

[21] P. Hannan, "The element-gain paradox for a phased-array antenna," *Antennas and Propagation, IEEE Transactions on*, vol. 12, no. 4, pp. 423–433, Jul 1964.

[22] N. Amitay, V. Galindo, and C. P. Wu, *Theory and Analysis of Phased Array Antennas.* Wiley-Interscience, 1972, p. 27.

[23] A. Ellgardt and H. Steyskal, "Antenna elements for wide-angle phased arrays," Division of Electromagnetic Theory, Royal Institute of Technology, Tech. Rep., 2005, TRITA-TET 2005:04.

[24] ——, “Study of waveguide elements for planar wide-angle scanning phased antennas,” Division of Electromagnetic Theory, Royal Institute of Technology, Tech. Rep., 2005, TRITA-TET 2005:05.

[25] S.-W. Lee, “Aperture matching for an infinite circular polarized array of rectangular waveguides,” *Antennas and Propagation, IEEE Transactions on*, vol. 19, no. 3, pp. 332 – 342, May 1971.

[26] S.-W. Lee and W. R. Jones, “On the suppression of radiation nulls and broadband impedance matching of rectangular waveguide phased arrays,” *Antennas and Propagation, IEEE Transactions on*, vol. 19, no. 1, pp. 41 – 51, Jan. 1971.

[27] G. N. Tsandoulas and G. H. Knittel, “The analysis and design of dual-polarization square-waveguide phased arrays,” *Antennas and Propagation, IEEE Transactions on*, vol. 21, no. 6, pp. 796 – 808, Nov. 1973.

[28] J. P. Montgomery, “Ridged waveguide phased arrays,” *Antennas and Propagation, IEEE Transactions on*, vol. 24, no. 1, pp. 46 – 53, Jan. 1976.

[29] C. C. Chen, “Wideband wide-angle impedance matching and polarization characteristics of circular waveguide phased arrays,” *Antennas and Propagation, IEEE Transactions on*, vol. 22, no. 3, pp. 414 – 418, May 1974.

[30] R. G. Schmier and M. J. Buckley, “Broadband circular waveguide radiating element for use in phased array antennas,” *AP-S*, vol. 2, pp. 1236 – 1239, June 1994.

[31] B. J. Lamberty, W. P. Geren, S. H. Goodman, G. E. Miller, and K. A. Dallabetta, “Wide angle impedance matching surfaces for circular waveguide phased array antennas with 70 degree scan capability,” in *Proc. Antenna Applications Symp.* Allerton Park, Sept. 2003, pp. 372–390.

[32] A. Ellgardt, “Study of rectangular waveguide elements for planar wide-angle scanning phased array antennas,” *Antennas and Propagation Society International Symposium, 2005 IEEE*, vol. 1B, pp. 815–818 vol. 1B, 2005.

[33] H. Wheeler, “The grating-lobe series for the impedance variation in a planar phased-array antenna,” *Antennas and Propagation, IEEE Transactions on*, vol. 14, no. 6, pp. 707–714, Nov 1966.

[34] B. Thors, H. Steyskal, and H. Holter, “Broad-band fragmented aperture phased array element design using genetic algorithms,” *Antennas and Propagation, IEEE Transactions on*, vol. 53, no. 10, pp. 3280–3287, Oct. 2005.

[35] H. Holter, “Analysis and design of broadband phased array antennas,” Ph.D. dissertation, KTH, 2000.

[36] B. A. Munk, T. W. Kornau, and R. D. Fulton, “Scan independent phased arrays,” *Radio Science*, vol. 14, no. 6, pp. 979 – 990, Nov.-Dec. 1979.

[37] J. J. Schuss and J. D. Hanfling, “Nonreciprocity and scan blindness in phased arrays using balanced-fed radiators,” *Antennas and Propagation, IEEE Transactions on*, vol. 35, no. 2, pp. 134–138, Feb. 1987.

[38] Y. Mushiake, “Self-complementary antennas,” *Antennas and Propagation Magazine, IEEE*, vol. 34, no. 6, pp. 23–29, Dec 1992.

[39] A. Neto and J. J. Lee, “Ultrawide-band properties of long slot arrays,” *Antennas and Propagation, IEEE Transactions on*, vol. 54, no. 2, pp. 534–543, Feb. 2006.

[40] ——, “‘Infinite bandwidth’ long slot array antenna,” *Antennas and Wireless Propagation Letters, IEEE*, vol. 4, pp. 75–78, 2005.

[41] R. Hansen, “Comments on ‘Infinite bandwidth long slot array antenna’,” *Antennas and Wireless Propagation Letters, IEEE*, vol. 4, no. 1, pp. 497–, 2005.

[42] X. Dardenne and C. Craeye, “Simulation of the effects of a ground plane on the radiation characteristics of self-complementary arrays,” *Antennas and Propagation Society International Symposium, 2003. IEEE*, vol. 1, pp. 383–386 vol.1, June 2003.

[43] M. Gustafsson, “Broadband array antenna using a self-complementary antenna array and dielectric slabs,” Lund Inst. Tech., Tech. Rep., 2004.

[44] N. Schuneman, J. Irion, and R. Hodges, “Decade bandwidth tapered notch antenna array element,” in *Proc. Antenna Applications Symp.* Allerton Park, Sept. 2001, pp. 280–295.

[45] M. Kragalott, W. R. Pickles, and M. S. Kluskens, “Design of a 5:1 bandwidth stripline notch array from FDTD analysis,” *Antennas and Propagation, IEEE Transactions on*, vol. 48, no. 11, pp. 1733–1741, Nov. 2000.

[46] D. H. Schaubert, “A class of E-plane scan blindnesses in single-polarized arrays of tapered-slot antennas with a ground plane,” *Antennas and Propagation, IEEE Transactions on*, vol. 44, no. 7, pp. 954–959, July 1996.

[47] ——, “A gap-induced element resonance in single-polarized arrays of notch antennas,” in *Antennas and Propagation Society International Symposium*, vol. 2. AP-S. Digest, June 1994, pp. 1264 – 1266.

[48] H. Holter and H. Steyskal, “Infinite phased-array analysis using FDTD periodic boundary conditions-pulse scanning in oblique directions,” *Antennas and Propagation, IEEE Transactions on*, vol. 47, no. 10, pp. 1508–1514, Oct 1999.

[49] A. Ellgardt, “A scan blindness model for single-polarized tapered-slot arrays in triangular grids,” *Antennas and Propagation, IEEE Transactions on*, vol. 56, no. 9, pp. 2937–2942, Sept. 2008.

[50] H. Holter, T.-H. Chio, and D. H. Schaubert, “Elimination of impedance anomalies in single- and dual-polarized endfire tapered slot phased arrays,” *Antennas and Propagation, IEEE Transactions on*, vol. 48, no. 1, pp. 122 – 124, Jan. 2000.

[51] H. Holter, “Dual-polarized broadband array antenna with BOR-elements, mechanical design and measurements,” *Antennas and Propagation, IEEE Transactions on*, vol. 55, no. 2, pp. 305–312, Feb. 2007.

[52] ——, “A new type of antenna element for wide-band wide-angle dual polarized phased array antennas,” *IEEE International Symposium*, Oct. 2003.

[53] E. Arnold, “A radiating element for an active airborne antenna,” in *Antennas and Propagation Society International Symposium, 1999.*, vol. 1. IEEE., July 1999, pp. 134 – 137.

[54] J. J. Lee, S. Livingstone, and R. Koenig, “A low-profile wide-band (5:1) dual-pol array,” *IEEE Antennas and wireless propagation letters*, vol. 2, pp. 46–49, 2003.

[55] ——, “Performance of a wideband (3-14 GHz) dual-pol array,” in *Antennas and Propagation Society International Symposium*, vol. 1. AP-S. Digest, June 2004, pp. 551 – 554.

[56] M. W. Elsallal and D. H. Schaubert, “Electronically scanned arrays of dual-polarized, doubly-mirrored balanced antipodal Vivaldi antennas (DmBAVA) based on modular elements,” in *Antennas and Propagation Society International Symposium.* AP-S. Digest, July 2006, pp. 887 – 890.

[57] T.-H. Chio and D. H. Schaubert, “A parameter study of stripline-fed Vivaldi notch-antenna arrays,” *Antennas and Propagation, IEEE Transactions on*, vol. 48, no. 6, pp. 879–886, June 2000.

[58] J. Shin and D. Schaubert, “A parameter study of stripline-fed Vivaldi notch-antenna arrays,” *Antennas and Propagation, IEEE Transactions on*, vol. 47, no. 5, pp. 879–886, May 1999.

[59] S. Kasturi and D. H. Schaubert, “Effect of dielectric permittivity on infinite arrays of single-polarized Vivaldi antennas,” *Antennas and Propagation, IEEE Transactions on*, vol. 54, no. 2, pp. 351–358, Feb. 2006.

[60] E. G. Magill and H. A. Wheeler, “Wide-angle impedance matching of planar array antenna by a dielectric sheet,” *Antennas and Propagation, IEEE Transactions on*, vol. 14, no. 1, pp. 49 – 53, Jan. 1966.

[61] D. M. Pozar, “Analysis of an infinite phased array of aperture coupled microstrip patches,” *Antennas and Propagation, IEEE Transactions on*, vol. 37, no. 4, pp. 418 – 425, Apr. 1989.

[62] D. M. Pozar and D. H. Schaubert, “Scan blindness in infinite phased arrays of printed dipoles,” *Antennas and Propagation, IEEE Transactions on*, vol. 32, no. 6, pp. 602 – 610, June 1984.

[63] D. M. Pozar, “General relations for a phased array of printed antennas derived from infinite current sheets,” *Antennas and Propagation, IEEE Transactions on*, vol. 33, no. 5, pp. 498 – 504, May 1985.

[64] R. E. Collin, *Field Theory of Guided Waves*, 2nd ed. IEEE Press, New York, 1991, pp. 705–707.

[65] J. Ramprecht, “Electromagnetic waves in media with ferromagnetic losses,” Ph.D. dissertation, KTH, 2008.

[66] D. Janning and B. Munk, “Effects of surface waves on the currents of truncated periodic arrays,” *Antennas and Propagation, IEEE Transactions on*, vol. 50, no. 9, pp. 1254–1265, Sep 2002.

[67] R. Lee and G. Smith, “An alternative approach for implementing periodic boundary conditions in the FDTD method using multiple unit cells,” *Antennas and Propagation, IEEE Transactions on*, vol. 54, no. 2, pp. 698–705, Feb. 2006.

[68] G. Turner and C. Christodoulou, “FDTD analysis of phased array antennas,” *Antennas and Propagation, IEEE Transactions on*, vol. 47, no. 4, pp. 661–667, Apr 1999.

[69] T. Martin, “Broadband electromagnetic scattering and shielding analysis using the finite difference time domain method,” Ph.D. dissertation, Linköpings Universitet, Linköping.

[70] L. Pettersson, T. Martin, and L. Pettersson, “FDTD with phase shift boudaries for simulation of infinite planar arrays,” in *Computational Electromagnetics - Methods and Applications, EMB04*, Gothenburg, Sweden, Oct. 2004, pp. 58–65.